A QUALITATIVE EXPERIMENTAL ANALYSIS OF LID-DRIVEN

CAVITY FLOW WITH SPLIT BOUNDARIES

By

Carrie K. Reinholtz

Thesis

Submitted to the Faculty of the

Graduate School of Vanderbilt University

in partial fulfillment of the requirements

for the degree of

MASTER OF SCIENCE

in

Mechanical Engineering

December, 2006

Nashville, Tennessee

Approved:

Professor Mark A. Stremler

Professor Deyu Li

Professor D. Greg Walker

To my husband, Todd, for his unconditional love, support, and patience.

ACKNOWLEDGEMENTS

I would first like to thank the Mechanical Engineering department at Vanderbilt University. Without acceptance into the program and financial support, I would have never had the chance to conduct this research nor meet the many people who have helped me along the way. I would like to personally thank the faculty, students, and personnel in the Mechanical Engineering Department whom I've had the pleasure of meeting along my journey. I thank you because you have provided me not only the educational foundation, but continued support and motivation to get me to where I am today.

I owe great amounts of thanks and gratitude to my thesis advisor, Dr. Mark Stremler. He has not only been an incredible educator, advisor, and confidant, but has provided me with lifelong advice in lessons both in and out of the classroom. Thank you for giving me the opportunity to work with you.

I give my most gracious thanks to each of my family members, my friends, and my loving husband. Without your continued love and support I would have never made it this far. I thank you for the many prayers and sacrifices you have made for me over the years. Please know that I am forever grateful.

TABLE OF CONTENTS

Appendix

LIST OF TABLES

LIST OF FIGURES

CHAPTER I

INTRODUCTION

Summary

The objective of this research is to perform a qualitative experimental analysis of two-dimensional, low Reynolds number incompressible flow in a lid-driven cavity. Although two-dimensional lid-driven cavity flow is not technically achievable in an experimental system, it can be approximated in three-dimensional space. Typically one dimension is much larger than the other two; this is the dimension that is considered infinite, and the dynamics of the system are looked at in an orthogonal two-dimensional plane. Studying two-dimensional flows under specific experimental conditions allows for further investigation into the flows' fundamental properties and is the main reason lid-driven cavity flow is frequently used to investigate computational and other mathematical models. Cavity flow is important both technologically and scientifically because it is able to display most of the intricacies of fluid flow in a geometrically simple environment [20].

Motivation

Scientists and engineers have been studying lid-driven cavity flows for over twenty years with continued success and improving accuracy [5]. These successes have been mainly due to the versatility of achievable flows, ranging from Stokes flow to higher Reynolds number flows, along with the ability to display many of the complexities

of fluid phenomena; from recirculating flows and corner eddies, to vortices and singular points [20]. Not only is lid-driven cavity flow important to the scientific world, specifically in fluids mechanics, but it has significant applications in industry, from processing foods and polymers [10] to coaters used to produce high-grade paper and photographic film [20].

In addition to the research and applications mentioned above, another motivation for this research is the ability this system has to display chaotic mixing [7]. With the introduction of chaos in the lid-driven cavity comes an efficient mixing scheme with the only moving parts being the boundaries that encompass the flow; no internally moving or turning mechanical structures need be present. The knowledge learned from this present research, in addition to enhancing the preliminary design, provides a starting point for developing new mixing approaches based on topological techniques (see Chapter II).

It is due to these numerous motivating factors that a variation of lid-driven cavity flow is considered (Figure 1). Adopting six moveable, discontinuous boundaries, as opposed to single or double wall-driven cavity flows, makes this research unique because it enables the display of flows not yet seen or studied before. For the scope of this experiment, only one of the six moving boundaries was studied, although the program developed for motor control was designed with the six moving boundary conditions in mind and can be utilized in the future.
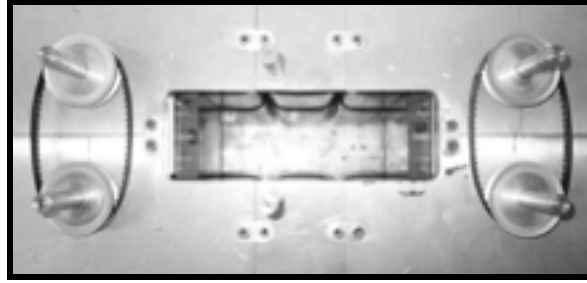
Figure 1. Top view of mixing tank showing the six moving boundaries on the top and bottom of the figure and the stationary boundaries located on the left and right of the center test cavity.

Background

Previous studies

Cavity flows, in general, have been a common experimental approach used to check or improve numerical or theoretical schemes. Weiss and Florsheim [23] were one of the first to study Stokes flow in rectangular cavities without a moving boundary. Using two different aspect ratios, they obtained approximate experimental solutions for flows over cavities and confirmed these results with their theoretical predictions.

Pan and Acrivos [16] were among the first to develop numerical techniques that predicted solutions for steady flows in rectangular cavities with a moving top wall and perform experiments for a variety of Reynolds numbers. Improvements to the numerical techniques have been a continual effort, but with Schreiber and Keller's work [18], they improved not only the reliability, but also the efficiency and accuracy. Even more recently, Bruneau and Saad [5] provide numerical results for both periodic and steady solutions.

In systems containing two moving boundaries, experiments using lid-driven cavity flows are useful in obtaining solutions or comparisons of predicted values [20], [9], [17], [12]. Kuhlmann , Wanschura and Rath [12] focused specifically on the non-uniqueness of two-dimensional flows, instabilities in two and three-dimensional flows, along with the formation of cellular structures. Lid-driven cavity flow, with two moving end-walls and free surface sidewalls, was used to model a roll coating system [9]. In this roll coating system, Gaskall, Gürcan, Savage and Thompson [9] determined that the analytic solution was easier to solve than with solid side walls. The predicted numerical streamlines proved to be in agreement with the experimental results.

With the increasing interest in mixing and chaotic advection, the lid-driven cavity also became a model for stirring devices. Chien, Rising and Ottino [7] studied laminar chaotic mixing in two-dimensional low Reynolds number cavity flows. Using two separate qualitative techniques, material line deformation and blob deformations, Chien et al. [7] study periodic and steady flows in the lid-driven cavity. Single boundary motion, along with motions in parallel and anti-parallel directions, made up the steady flow cases. Time periodic experiments were performed on different cases, including periodic discontinuous boundary operation and periodic flow that incorporates a phase angle to offset the two boundary velocities. The steady flow cases prove to be an effective way to display the streamline dynamics of the system. The two time-periodic cases improved the mixing. Fewer time periods are needed for decent mixing to occur compared to other studies done in journal bearing flows. Ottino [15] later published improved results from this experiment using a computer-controlled system.

End wall effects in lid-driven cavity flows were studied by Prasad and Koseff [16]. By measuring velocities in a square cross section, they were able to quantify the effects of varying the Reynolds number and the spanwise aspect ratio (SAR). SARs have a strong effect on the flow in the cavity, and as the Reynolds number changes these effects are quite different. It is from these studies that Prasad and Koseff [17] recommend no larger than a 3:1 aspect ratio (see Figure 5 in Chapter 2). If this ratio is exceeded, Taylor-Goertler like vortices form and the flow becomes three-dimensional.

From an electromagnetic perspective, lid-driven cavity flow was simulated using a magneto hydrodynamic (MHD) mixer, developed and tested by Bau, Zhong, and Yi [3]. The MHD device applies alternating potential differences across a pair of electrodes, inducing a current in a conduit filled with an electrolyte solution. When performed in the presence of a magnetic field, body forces are induced which causes the fluid inside the channels to move in complex motions. This motion stretches the material surfaces, enhancing the overall mixing of the fluid and shows that lid-driven cavity flow is not restricted to systems involving a physically moving boundary. This research showed success in using induced currents in magnetic fields for mixing fluids without any moving parts.

Generating Topological Chaos

Boyland, Aref and Stremler [4] studied topological mixing schemes with physical stirring rods both theoretically and experimentally. Using three (or more) stirring rods, two different periodic motions can be created: one that can produce exponential stretching and deformation of the fluid, known as topological chaos, while a second does

not have these same characteristics (Figure 2). The motivation behind this research is

the goal of generating a fluid motion in a lid-driven cavity that is analogous to the flow

illustrated in Figure 2(f).
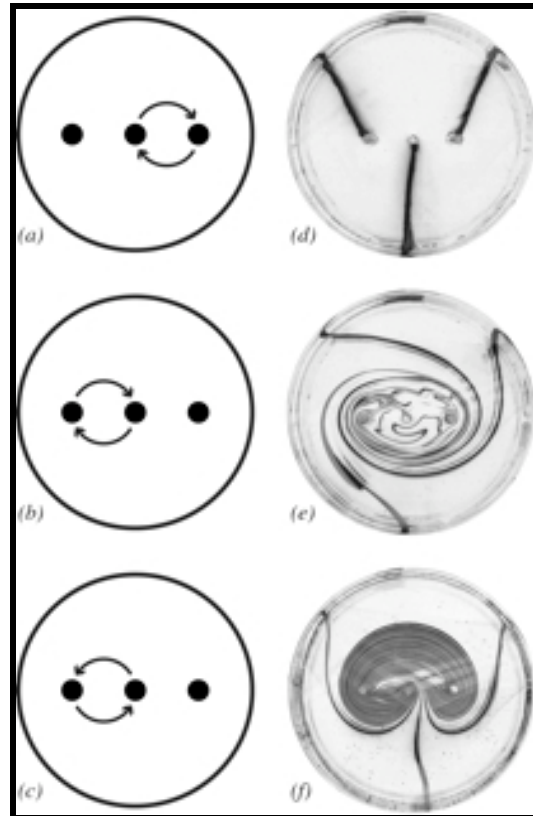
Figure 2. Images taken from the research conducted by Boyland, Aref and Stremler [4]
showing the two different protocols created using three stirrers. The first interchange for
both protocol (a,d) and the second interchanges for the scheme that does not produce
topological chaos (b,e) and the schemes that do (c,f).

The research presented within this document was established as an experimental

approach to complement the numerical solutions currently being developed by Chen [6],

which provided a starting point for the experimental velocities and time scales used in

this research. Chen is developing a numerical approach to solving the Navier-Stokes equation under the assumption of Stokes flow, for an incompressible viscous fluid in rectangular cavity flow. The geometry and some streamline solutions are shown in Figure 3.
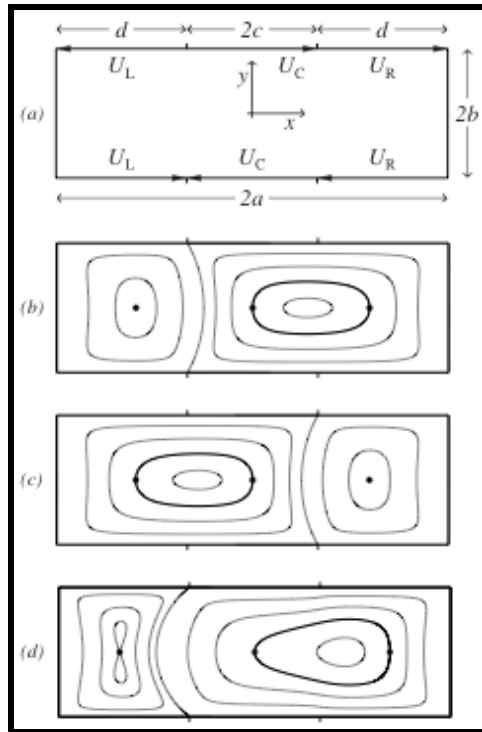
Figure 3. This diagram, adopted from Chen's [6] work, shows both the test section geometry (a) and sample streamline solutions (b-d). The first interchange (b) is for both protocols. Using a second interchange (c) in the same direction as (b) gives non-topological chaos creating scheme; in the opposite direction gives the scheme that produces topological chaos (d) – a case in which the leftmost rod is a hyperbolic stagnation point rather than elliptic as in (b).

Governing Equations

Lid-driven cavity flows have been a continued topic of research in the fluid mechanics community for years due to the simple geometry and well-defined boundary conditions [19]. Fluid motion inside the cavity is governed by the continuity equation and the Navier-Stokes equation, defined as the following:

$$\nabla \cdot \mathbf{V} = 0 , \tag{1}$$

$$\rho \frac{D\mathbf{V}}{Dt} = \rho\left(\mathbf{V}_t + (\mathbf{V} \cdot \nabla)\mathbf{V}\right) = -\nabla p + \mu \nabla^2 \mathbf{V} . \tag{2}$$

where, ρ, V, and p represent the dynamic viscosity, velocity, and pressure respectively and the body forces have been included in the pressure term. Lid-driven cavity flow assumes two-dimensional, incompressible, viscous fluid flow and drastically simplifies the full, three-dimensional Navier-Stokes equation. Boundary conditions are dictated by the employed velocity distribution, whether stationary or moving.

Nondimensionalizing and choosing the appropriate viscous pressure scale that reduces the pressure coefficient to unity gives:

$$Sk\mathbf{V}_t + \mathrm{Re}(\mathbf{V} \cdot \nabla)\mathbf{V} = -\nabla p + \nabla^2 \mathbf{V} , \tag{3}$$

where two new dimensionless parameters have been introduced, the Stokes number (Sk) and the Reynolds number (Re). Both numbers represent ratios with the Stokes number being the ratio of the local or transient inertia to the viscosity, whereas the Reynolds

number relates the convective inertia to viscosity. Equation 4 is valid for flows where viscous forces predominate and when Reynolds numbers are small.

The Stokes number reduces to zero since viscous forces in lid-driven cavity flow dominate over local inertial forces in the system, further reducing Equation 3:

$$\mathrm{Re}\left(\mathbf{V}\cdot\nabla\right)\mathbf{V} = -\nabla p + \nabla^2\mathbf{V}, \qquad (4)$$

leaving the governing equation dependent only on the Reynolds number and pressure terms. The Reynolds number is an important parameter in all viscous flows because it determines whether the flow conditions are laminar or turbulent, and is defined by the following relationship:

$$\mathrm{Re} = \frac{VL}{\upsilon}, \qquad (5)$$

where V is the velocity scale, L is the length scale and ν is defined as the kinematic viscosity or viscous diffusivity [23]. Reynolds number calculations for this research will be discussed in Chapter 2.

Applying the assumptions of two-dimensional flow (x-y plane), the streamfunction, Ψ, can be introduced to satisfy continuity:

$$u(x, y) = \frac{\partial\Psi}{\partial y}, \qquad (6)$$

$$v(x, y) = -\frac{\partial \Psi}{\partial x}, \tag{7}$$

where the streamfunction both simplifies the analysis and has physical significance. Streamlines are everywhere perpendicular to the velocity and act as boundaries, in the sense that no mass flow occurs across streamlines.

The vorticity is ω and is defined as the curl of velocity:

$$\omega = \nabla \times \mathbf{V}. \tag{8}$$

For 2-D flows the vorticity is perpendicular to the x-y velocity (in the direction of z) and can be written as:

$$\omega = \left(\frac{\partial v}{\partial x} - \frac{\partial u}{\partial y} \right). \tag{9}$$

Combining equations (6), (7), and (9), results in the following:

$$\nabla^2 \Psi = -\omega. \tag{10}$$

Under the assumption of Stokes flow (Re <<1) the viscous effects dominate over the inertial effects further reducing equation (4) to the 2-D biharmonic equation:

$$\nabla^4 \Psi = 0. \tag{11}$$

It is not a goal of this research to solve the governing equations, but to familiarize the reader with the governing flow equations and how lid-driven cavity flow simplifies an otherwise intricate three-dimensional equation. Chen is conducting a numerical analysis using particle tracking techniques to look at topological chaos in Stokes cavity flow with six discontinuous moving boundaries [6]. This research uses some preliminary findings from Chen's work as a starting point for establishing both periodic time intervals and wall velocities.

CHAPTER II

EXPERIMENTAL SYSTEM

Summary

This chapter outlines the design and setup of the experimental lid-driven cavity system. There are two main parts to the experimental system: the physical mixing device and the computer control program. The cavity device has been in development for several years and is a collaboration of effort from previous graduate and undergraduate students. Prior to the research presented herein, neither the design nor the computer program was fully operational. Several modifications needed to be implemented to improve the device and the motor controls. These changes included modifications to the physical tank, the electrical operating components, and the LabVIEW program. This chapter discusses the experimental system and also describes how the experimental design incorporated the constraints of each components and how the device was calibrated to obtain repeatable results.

The variation of lid-driven cavity flow considered in this research consists of two parallel walls, split into three separate sections, for a total of six movable boundaries. Each wall is able to move in positive and negative directions, allowing numerous flows to be created in the lid-driven cavity (Figure 4). For the scope of this experiment, a preliminary case was studied in which only one of the six moving boundaries was used. Parallel walls were designed to always move in opposite directions; therefore only three motors are needed for the setup and makes for a more simple control program. A

LabVIEW virtual instrument was created to control the motors of the mixing device and was designed in such a way to activate all six moving boundaries, even though only one wall is being used for the current work. The control program can be utilized in the future to provide velocity distributions that will produce the topological mixing schemes presented in Chapter 1.
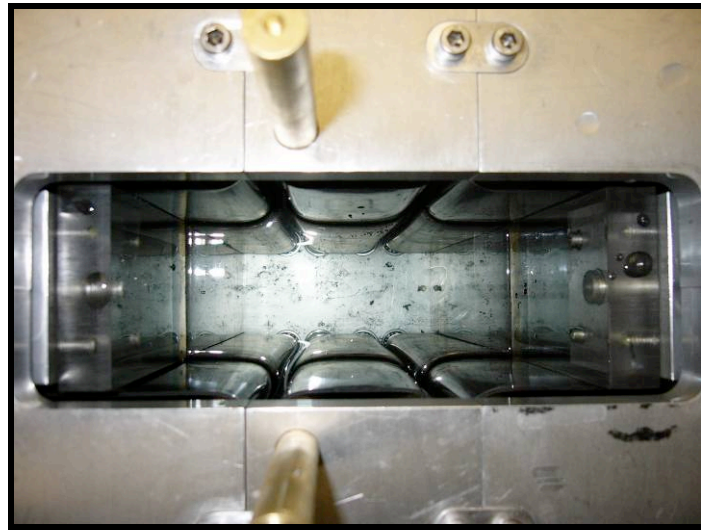
Figure 4. A close-up, top-down view of the test section showing the six discontinuous boundaries, two center driving rods, and the glycerin-filled center cavity.

Experimental Design

Fluid tank

The stirring device designed for this research consists of a glycerin filled aluminum tank constructed from aluminum plating (Figure 5). Two sidewalls are overlaid with acrylic windows, providing a view of the inside of the tank. The six boundary sections are separated by a center test region of 2.75 inches (Figure 6) and in the cases studied throughout this experiment, each of the moveable boundaries measure 2.75 inches in width for a total test section length of 8.25 inches. The 3:1 aspect ratio follows the recommendations of Prasad and Koseff [16] in order to maintain essentially two-dimensional flow without the development of secondary structures. A depth of approximately one foot was used based upon the work conducted by Ottino [15] although the aspect ratios differed. This depth was chosen to allow for two-dimensional assumptions to still govern the flow.

Two stationary boundaries, made out of half-inch acrylic, enclose the movable walls in the test region. These acrylic walls correspond to the window on the external structure of the tank so the center test region is fully visible from the outside of the tank. A cutout on the top of the tank reveals the inside entire test region and allows access for dye insertion and photographs to be taken of the test region (Figure 4).

Figure 5. Side view of glycerin filled tank showing the
structure, acrylic sidewalls, and adjustable sidewalls.
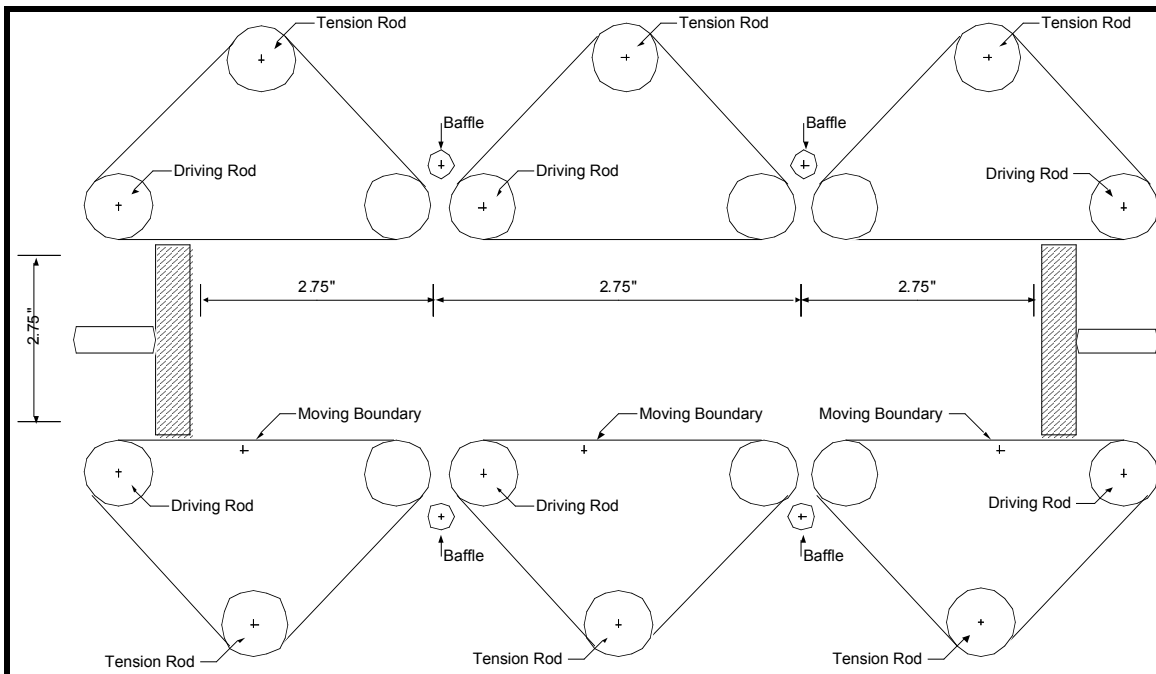
Figure 6. A schematic of the internal components of the tank (not to scale).

Each moving boundary is constructed from a sheet of neoprene formed into a long belt

and fastened around a set of three rods. These three rods create long, triangular tubes,

15

and the base of each of these triangles forms the moving wall as shown in Figure 7. One of the three rods is the driving rod, which is mounted in ball bearings and connected to the motor via a gearing system.

Figure 7. Side view of cavity system looking parallel to the
internal moving boundaries as viewed by the observer.

A second rod, also mounted in bearings, keeps the boundary moving and is attached to the driving rod via a gear and pulley system, as shown in Figure 11. The third rod acts as a tensioner, pulling the moving boundary snug against the other two rods and keeping the wall smooth and straight. The driving rods in opposing wall segments are attached to the same motor but are assembled such that they rotate in opposite directions. In other words, opposing boundaries move with the same velocity but in opposite directions.

This experimental device has been designed so that it has the ability to create two different stirring protocols. Figures 8 and 9 show the geometries and velocity configurations that result in two different mixing protocols, where only one produces topological chaos. Using the six movable boundaries, periodic points are created and interchanged in the flow by driving the walls with certain velocities [6]. These periodic points are interchanged along streamlines in the flow. Once there is successful experimentation with a single moving split boundary, the next step is to utilize all six boundaries to study the two stirring protocols.
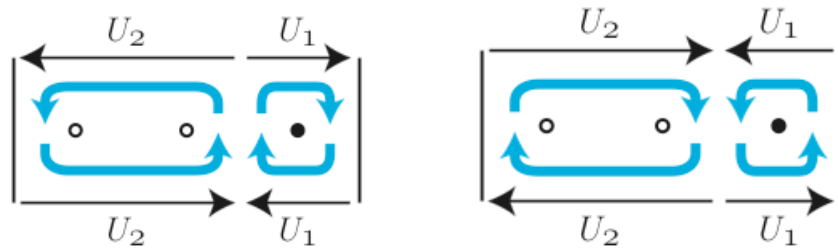
Figure 8. The first and second interchanges of the non-topological chaos producing scheme.
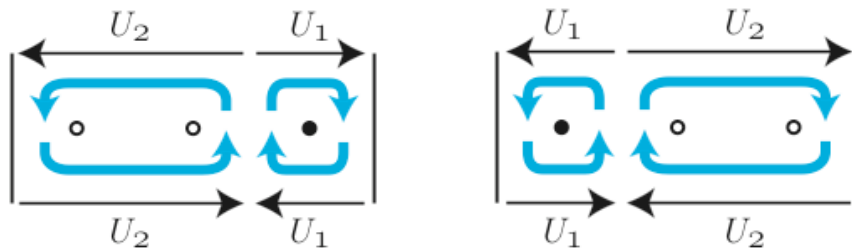
Figure 9. The first and second interchanges of the stirring scheme that produces topological chaos after three periods or six interchanges.

System constraints

Two constraints dictate the attainable system velocities: Reynolds number and minimum operational motor frequencies. These two quantities are related through the belt velocities, which are calculated from gearing relationships and gear radii:

$$v_i = 2\pi\omega_i R_i, \tag{12}$$

with, v the velocity measured in meters per second, ω the frequency measured in revolutions per second, and r the radius of the gear measured in meters. The subscript denotes the gear number.

A side view of the gearing system is shown in Figure 10. Gear 1 is attached to the motor and planetary gear head, gear 2 and 3 are fastened to the driving rod of one boundary, and gear 5 attaches the two driving rods of the boundaries. Gears 4 and 6 are the radii of the rods and the final determining factor of the belt velocity. The thickness of the neoprene walls was considered negligible in these calculations. Table 1 shows the radii of all of the gears.
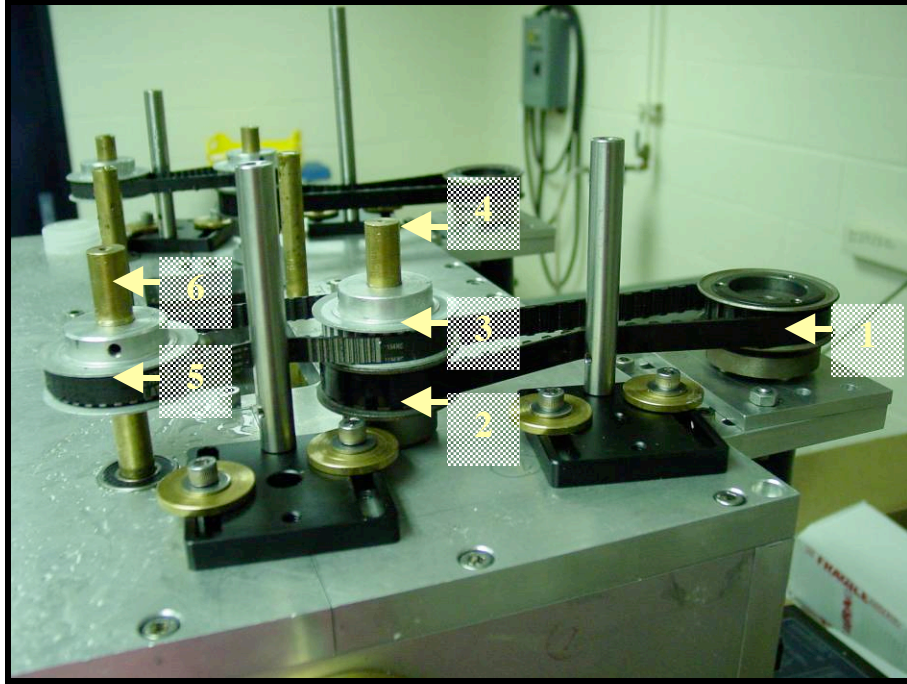
Figure 10. A side view of the motor gearing system that drives parallel walls with equal velocities. Each gear is labeled with its identifying number.

Since gears 1 and 2 are attached via the same belt, their linear velocities are equal. Furthermore, gears 2, 3 and 4 rotate with the same frequency since they all rotate about the same axis; the same is true for gears 5 and 6. Since the radii of gears 2, 3, and 5 are all the same, then the linear velocities of gears 3 and 5 are equal. The final belt velocity comes from the following relationships:

$$v_4 = \frac{R_4}{R_2} v_1 = \frac{R_4}{R_2} 2\pi\omega_1 R_1 = \frac{R_4}{R_2} 2\pi\omega_{motor} R_1 \tag{13}$$

According to the Maxon motor specifications, the minimum operating frequency is 60 revolutions per minute, or 1 revolution per second. This limits the minimum allowable

19

ω_1. Based on this limitation and the values given in Table 1, the minimum achievable boundary velocity is $v_4 = 0.0678$ m/s.

Table 1. Gear radii dimensions in both inches and mm.

Gear	Radius [in]	Radius [mm]
R_1	1.0625	26.9875
$R_2 = R_3 = R_5$	0.9375	23.813
$R_4 = R_6$	0.375	9.525

The length and velocity scales (L and V, from Equation 2) are two of the parameters for the Reynolds number calculations that have now been established. The only parameter unaccounted for is the kinematic viscosity. Glycerin was the chosen fluid for this experiment because of its high viscosity. The viscosity of glycerin is temperature dependent and, due to the circumstances presented in the laboratory, the lowest achievable temperature was 30°C. At 30°C, the kinematic viscosity of 96% glycerin is equal to 0.000223 m²/s, resulting in a Re ≈ 20.

It was a goal of this experimental research to operate with Re << 1 in order to compare with the mathematical analysis that assumes Stokes flow. However, due to the operating temperatures and properties of the governing fluid this goal was not achieved. With an operating Reynolds number of approximately 20, Stokes flow assumptions are invalid, but the flow is still laminar, and still capable of producing important results and giving insight for continued research.

Chen [6] determined a velocity ratio of 1:1.9688 was needed to produce topological chaos in the flow. This velocity relationship is needed to determine the other

boundary velocities. Because of the restrictions presented previously, the velocity obtained above has to be equal to the lower bound in the velocity ratio. V_{low} has a value of 0.0678 m/s and V_{high} must be 1.9688 times greater than $V_{low,}$ giving V_{high} = 0.1335 m/s. These values will become important when multiple boundaries are used. If the upper limit of the velocity is used, which is not applicable in this research, the smallest achievable Reynolds number would be approximately 40.

Tank Modifications

A gap exists between the neoprene wall segments due to the diameter of the bearings installed to hold the driving rods. This poses a problem because once the boundaries start to move, fluid easily flows out of these gaps. One solution is to use baffles to restrict the fluid flow out of these gaps, thus decreasing the amount of fluid escaping the center test region. Four baffles, constructed out of all-thread, span 24 inches of the fluid depth and attach to the tank sidewalls. They are installed 1/8" from to the gap midpoint and designed to not interfere with the neoprene walls. The baffles create a barrier on the exterior side of the test region, decreasing the overall fluid loss. Although some fluid still escapes, the baffles are considered the best solution, given the design of the system. Other resolutions would have been costly and difficult to implement without redesigning the entire system.

Another modification made to the tank design was the addition of a tensioning system for each of the motor gearing systems. The belts that connect the motor gearing system have a large amount of slack. This slack allows the belts to slip and as a result the rods do not turn inside the tank. The tensioning system consists of optical mounting rods

that tighten each of the belts enough to allow smooth driving of the gears. Six of these tensioning systems are installed on the mixing device.
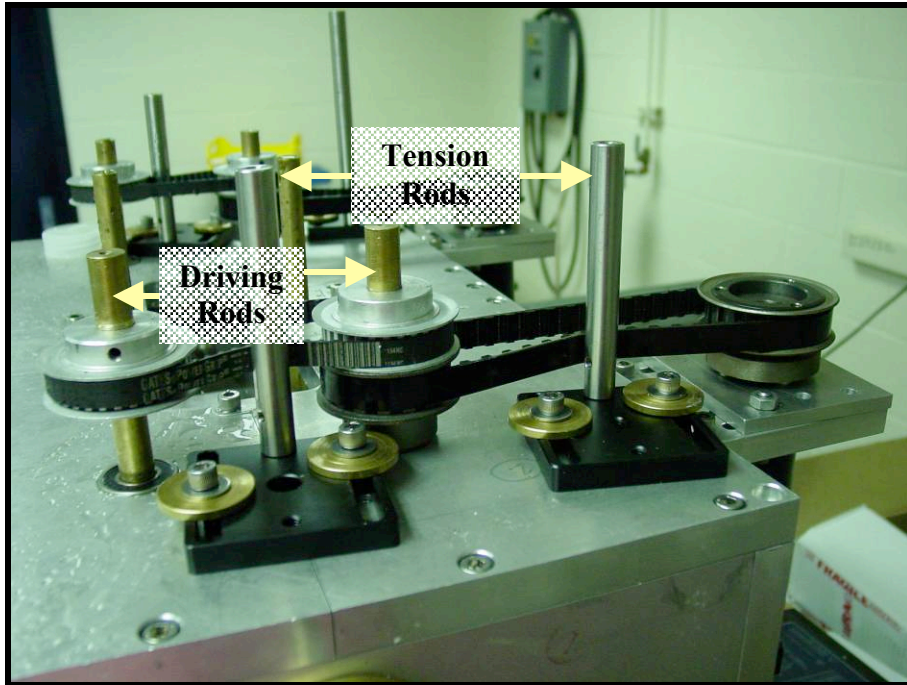
Figure 11. A side view of the motor gearing system in which the tensioning system and driving rods are labelled.

The two final modifications are minor but worth mentioning. The interior floor of the tank was painted white to reduce glare from camera flash and provide contrast between the bottom of the tank and the dye. The preliminary draining mechanism was impractical; using a bolt screwed to the bottom of the tank, and when unscrewed completely, would empty the 10 gallons of glycerin. The improvement consisted of a plumbing fitting that attaches the tank to a six foot long section of flexible tubing with a ball valve attached to the end. This allows for convenient and variable draining of the glycerin-filled tank.

Control Program and Components

The motor control program was created using a LabVIEW virtual instrument. The user defines the system parameters, namely velocity, acceleration and final position, on the front panel of the program (Appendix A) and then executes the program to run for the time dictated by the input parameters (Figure 12). Once these parameters are set, the program sends a signal to a four-axis National Instruments NI MID-7654 servo motor (Appendix B). For this experiment, only three of the four axes are used. Before the servo motor is connected to each of the three Maxon RE40-148877 DC motors the computer signal is first sent through a choke, an encoder, then to the motors (Appendix C).

In a previous study, the motors had a tendency to overheat making them inoperable until they cooled. It was determined that a choke was needed for the three motors to increase the motor terminal inductance and decrease the current ripple (Appendix D). A Maxon Tacho HEDL 55 digital encoder was installed on each of the motors to accurately measure the motor's position which, in turn affects the output velocity (Appendix E). The motors attach to a GP 42 C planetary gearhead (Appendix F). See Figure 13 for the schematic of the entire system.
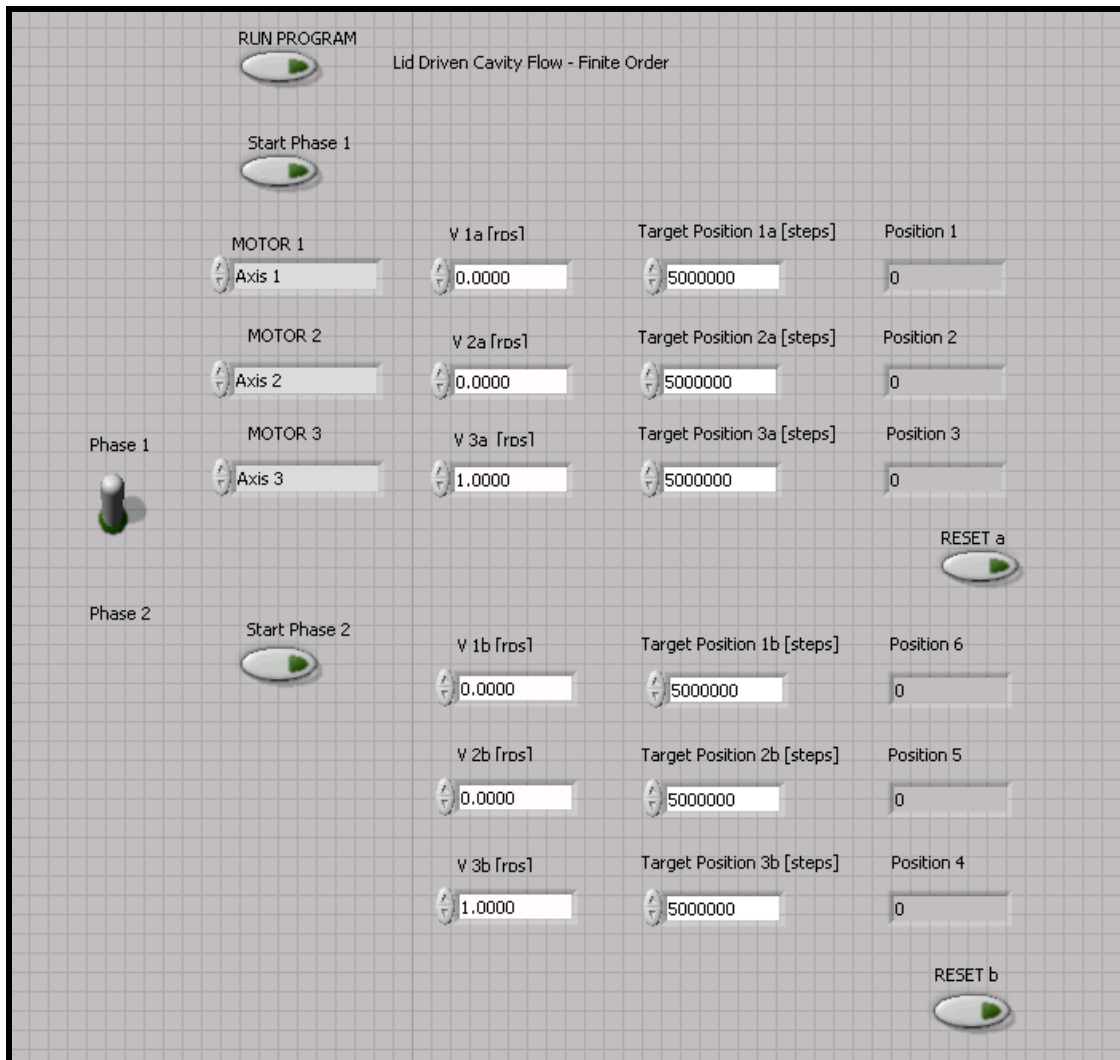
Figure 12. LabVIEW front panel diagram showing input parameters: velocity and target positions, for each of the three motors.
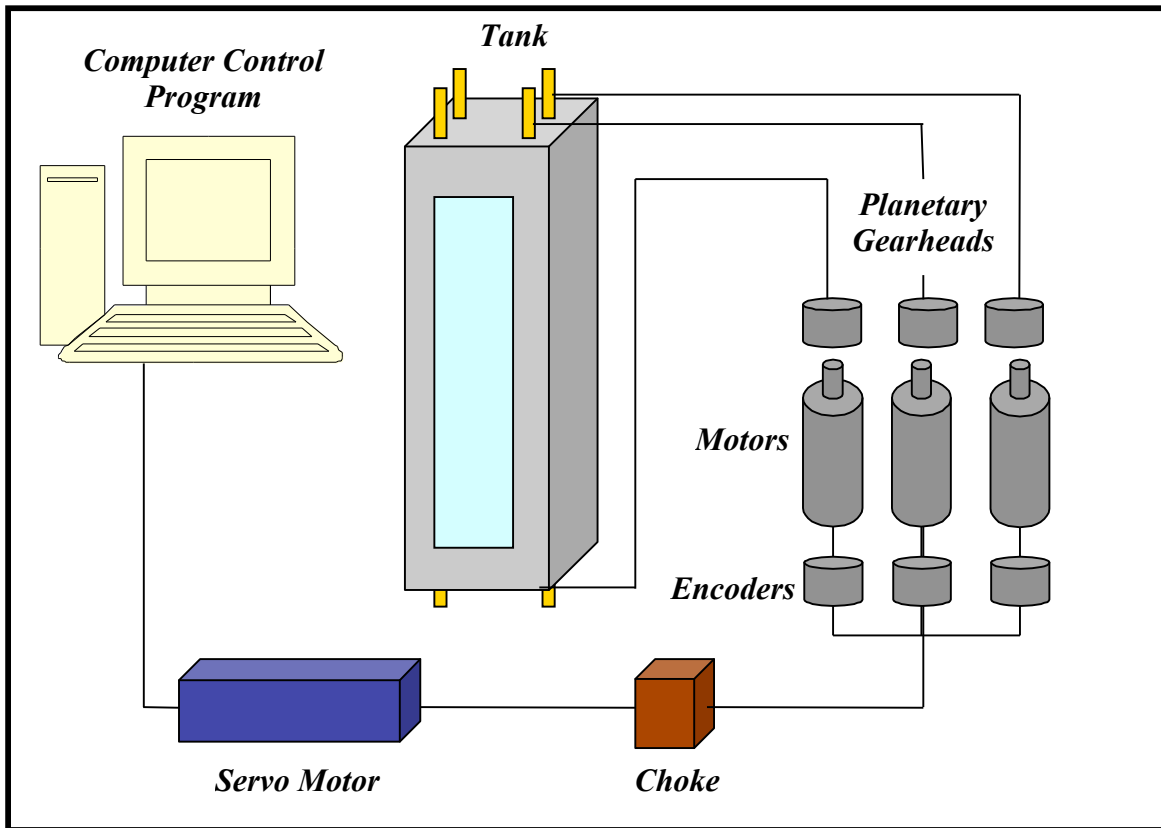
Figure 13. Overall schematic of the system showing each specific component. The computer is connected to the motors first through the servo motor, the choke, then the encoders. Each of the motors has a planetary gear head that attaches to the top before connecting to the gearing system.

Motor Calibration

In order to produce both accurate and repeatable results, each motor is calibrated before running any experimental analysis. Because three different motors were used to drive the boundaries, it is important that for each motor the values entered into the program provide the accepted velocities at the moving boundaries. The motors are calibrated by setting a velocity within the LabVIEW program, choosing the number of revolutions and recording how long it takes to complete these revolutions. These values

are then used to set the gain in the motor control program. Performing the calibration for

each of the three motors, accounts for differences between the motor's output velocities.

CHAPTER III

EXPERIMENTAL ANALYSIS

Summary

The purpose of this chapter is to outline some of the steps taken throughout the experimental setup and procedure; specifically identifying some important adjustments to consider to ensure the system will function properly.   If these adjustments are not performed, it can cause damage to tank components.   This chapter also presents the operating conditions for each of the three separate cases performed in the glycerin-filled tank, followed by a discussion of the results for each case.

Procedure

Before adding the glycerin to the test cavity, the boundaries should be tightened. This way only minor adjustments need to be made to the moving belts after the glycerin is added. By tightening each of the tension rods, the moving boundaries will flatten and create the rectangular test section. During this adjustment period, it is critical that the moving wall is adjusted parallel to the tank walls. Otherwise, it will cause the boundary to creep either up or down the driving rod, creating a slight velocity in the z-direction, which in turn will create small secondary flows. If the boundary starts creeping up and down and catches on the mechanical components, it can rip the neoprene sheet. If this were to happen, the entire system would have to be drained and disassembled to replace the damaged neoprene belt, which is a very time consuming process.

27

The motor control program is then run continuously to ensure the correct motor is running in the designated direction. If the belts slip, the tension rods are adjusted until the belts are moving again. Once the belts are moving smoothly, the motors are stopped and the glycerin is added to the tank. Approximately ten gallons of glycerin was used for the experimental results presented. The maximum capacity for the tank is around 15 gallons. After the tank is filled, the LabVIEW program is run again and minor adjustments are made to the moving boundaries before any runs are started. Once the belt is moving without slipping or stalling the motors, dye is inserted into the test cavity for the start of the experiments.

The dye used in the following trials is a mixture of food coloring and glycerin. This was done to preserve the viscosity of the fluid, such that the dye tracers follow the fluid flow. Three spots of colored dye were used, one in each tank section, and were injected just under the top surface of the cavity without disturbing the flow.

Results

Three separate runs were conducted for this research. For all of the runs, the operating motor was set to operate at 1 rps, corresponding to a linear belt velocity of ±0.0678 m/s, depending on the case. The moving belt is located in the bottom left-hand corner for all of the images in all of the runs. The time period adopted for the runs was equal to, or a multiple of, the calculated dimensionless period from Chen's work, 7.186. This is a dimensionless value that corresponds to the dimensionless velocity value calculated to be 1.9866. To convert Chen's dimensionless variables into experimental values, the product of his two dimensionless variable need to be set equal to a

nondimensionalized version of the experimental variables. This was done using the relationship:

$$1.9688 \cdot 7.186 = \frac{V}{D} \cdot T \,, \qquad\qquad (14)$$

where V is the high-speed belt velocity, V_{High} in m/s, D is the characteristic length in meters, and T is the period in seconds. Solving for T, yields a value of 7.402 seconds. Since only the lower velocity was employed during these studies, the operating Reynolds number is approximately 21. Images are taken after each segment using a digital camera.

Case I

Figure 14 shows the initial location of the three glycerin dots. Three colors were used to make it easier to keep track of the fluid motion. The lower left boundary is driven to the right, as indicated by the arrow, for a period of 7.4 seconds, and the resulting dye distribution is shown in Figure 15. Since there is only one moving boundary on the left side of the tank, the fluid motion on the right hand is minimal. This means there should not be a lot of movement in the green dye spot. After one period the two left hand spots do move to the left, while the green dot on the right has shifted a minimal amount.

During this case, the moving belt slipped before the completion of the one time period. The belt tension was adjusted before running another period in the same direction as the first, and further slipping did not occur.
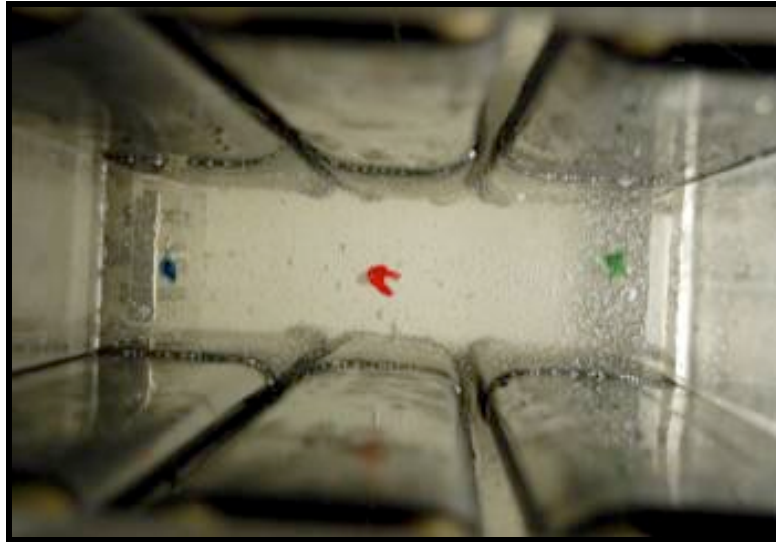
Figure 14. Initial positions of glycerin tracer spots before any boundary motion occurs. For readers viewing these images in grayscale, the dots are arranged as blue (left), red (center), and green (right).
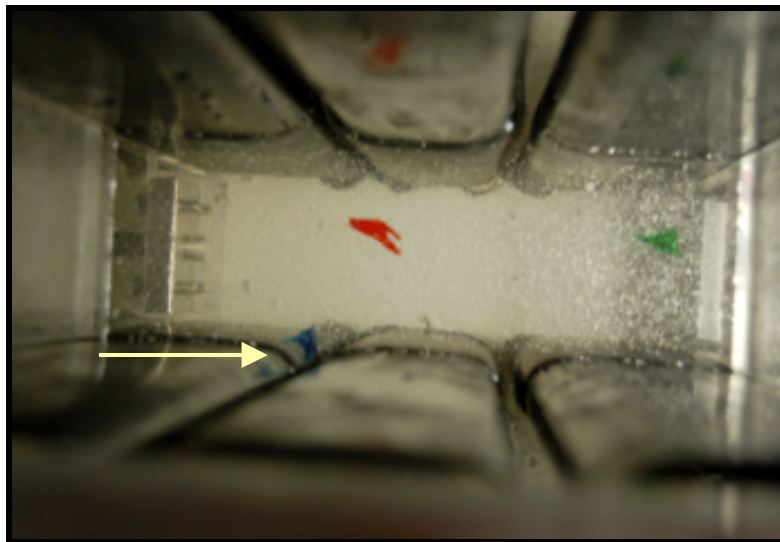
Figure 15. Image showing fluid movement after one time period of the lower left boundary moving to the left, as indicated by the arrow.

After the second period, the fluid motion becomes more apparent as shown in Figure 16. The red fluid has moved further left, to the opposite side of the blue dot. The blue dot and red dot seem to be concentric, tracing out similar paths at a similar distance during the entire period. This is to be expected since the flow is laminar. Similar to the prediction, the green dot migrates only slightly to the left due to the motion of only one boundary. Fluid is escaping due to the wall motion where the moving boundary meets up with the non-moving wall. Because fluid is escaping the test cavity while the depth of the glycerin remains unchanged, it can be concluded that fluid is also entering the test cavity through the other gaps at the same rate it is leaving. Baffles were implemented to decrease the amount of fluid exchanged between the test cavity and the ambient fluid, but these baffles did not eliminate the fluid flux.
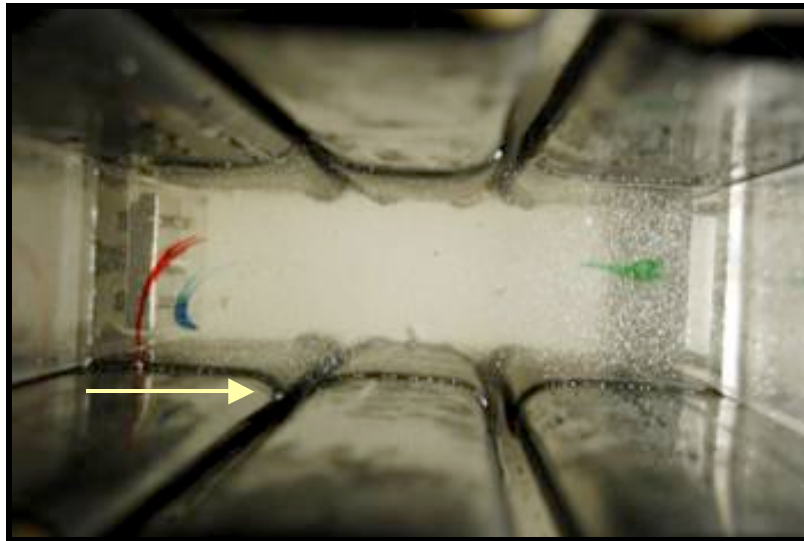
Figure 16. Movement of fluid after two time periods, but after some slipping occurred during the first period.

After a third time period, for a total run time of 22.2 seconds, with the belt moving still in the same direction, the red fluid tracer has disappeared while the blue dye is still present (Figure 17). The red dye escaped through the wall gap while the blue-dyed fluid continued tracing out a streamline arriving almost back at its original starting position. Because the red dye was pulled out of the center test region after the second period shows there is a fair amount of fluid being pulled from the center section. Again, the green dye is being stretched slightly to the left, which is probably a result of the induced velocity from the moving boundary and the loss of fluid through the boundary gap.
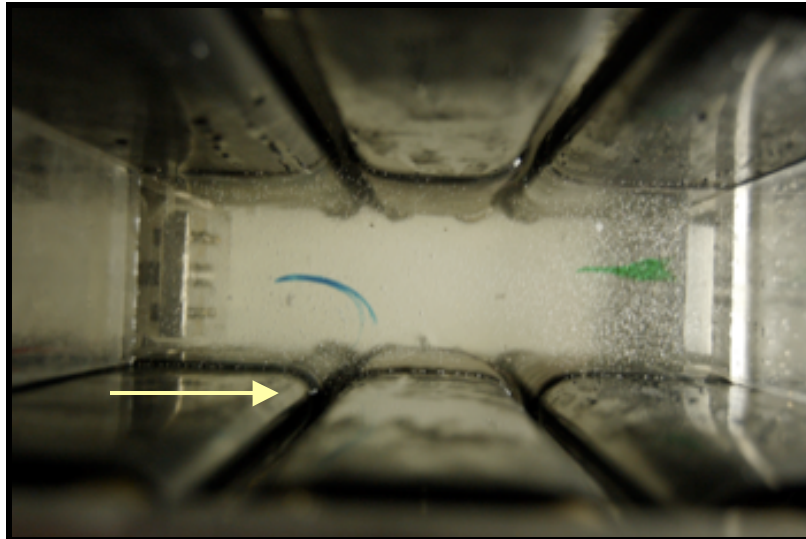
Figure 17. The last segment of Case I executed for third and final time period. Notice the red dye has disappeared and the blue dye has traced almost 360 degrees back to its original starting position.

Case II

A second case was run with the same belt velocity as in the first case but with a period twice as long, 14.8 seconds. Figure 18 displays the originating locations of each of the three dots. Note that the original location of the blue and red dots has been interchanged relative to case I (Figure 14). This was done because the red dot has better contrast with the tank bottom, and the center dot eventually escapes through the boundary gap.
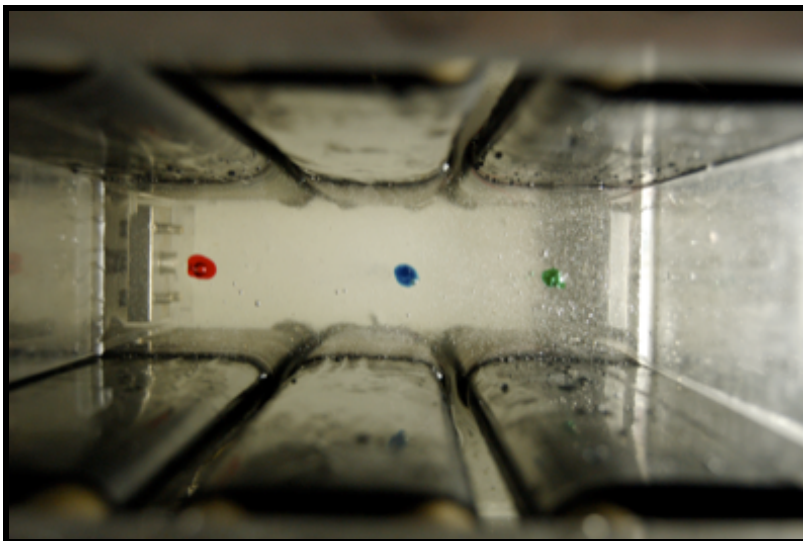
Figure 18. Initial starting locations for the second case. Note that the original locations for the blue and red dots have been interchanged, red (left), blue (center) and the green dye location remains unchanged.

After two time periods, the results are similar to those presented in the first case; although this time with more clarity and less error (Figure 19). Here, the red dot moves from the center of the test region and travels on a path that is almost concentric to that

traced by the blue fluid particles. This is expected, since streamlines do not intersect in steady flow. The original starting location of the red dot also migrated down and to the right (from the perspective captured in the photograph). This is due to the fluid loss out of the gap between the moving and stationary boundary. As expected, there is very slight movement in the green dot.
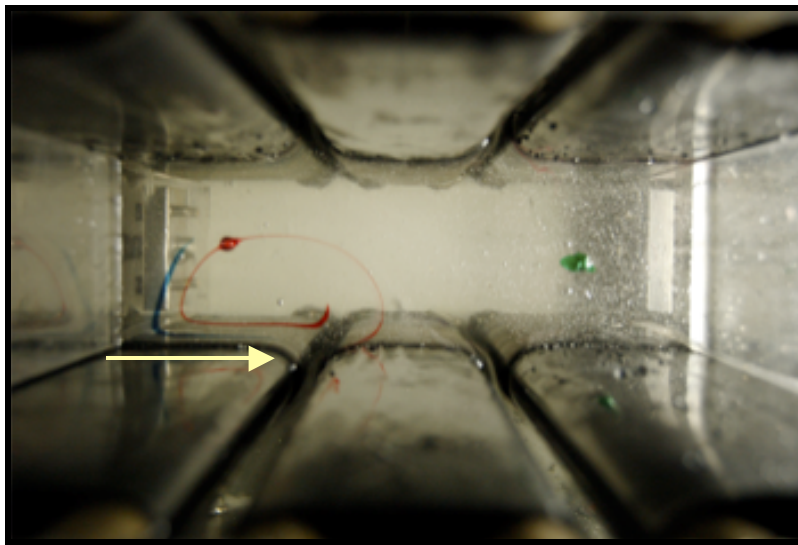
Figure 19. Boundary motion for the duration of two consecutive time periods.

The second segment for case two is the same as the first, consisting of another two time periods of continuous operation with the same wall velocity. Due to the longer duration in time, more motion is seen in the fluid (Figure 20). First, the blue dye has completely disappeared, as with the red dye in the first case. This is because the blue dye travels along the boundary of the wall and is contained within the fluid that is forced out between the wall gaps. Although very slight, there is a small movement in the green

fluid, even less than what was seen in case I (Figure 16). The difference can be attributed

to a difference in the original locations of the dots, as they may have differed slightly for

each case. A change in initial position would result in the fluid particles following a

different streamline and tracing out a different trajectory. This presents a point to

consider in the in future research. If multiple runs are used for a particular test case,

identical volumes of dye should be used in the same locations, guaranteeing the tracer

particles follow the same streamlines for each run. If operating conditions differ, this

technique will allow for direct comparison of the fluid motion between cases.
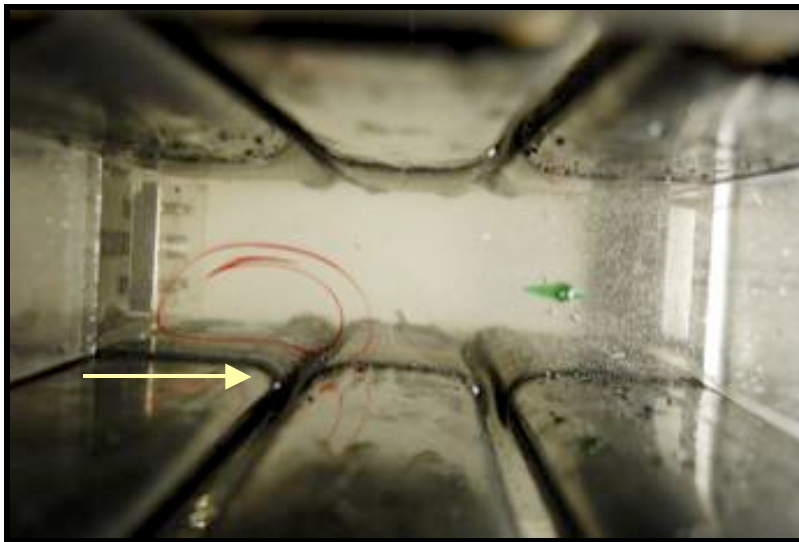
Figure 20. Results after operating tank for a total of four time periods
with the arrow indicating the boundary motion.

One might expect to see the red dye continue around in a single trajectory, due the

single boundary motion. However, this is not the case since fluid is being exchanged

between the test section and the ambient outer fluid. If operation were to continue, it

appears that the particles may continue to circle inward, rather than follow a single closed trajectory.

Running for yet another sequence, at the same velocity and for twice the calculated period, the results begin to differ from the prediction that the particles would continue circling inward (Figure 21). There is still no presence of the blue dye, meaning the entire dot escaped through the break in the boundaries. The fluid once again continues to circulate around the previous half-circle-like trajectory, ending just above the gap between the two walls. During this period the results of the fluid escaping through the gap becomes apparent. The red lines that were present in the last sequence begin to escape through this crack, distorting the trajectory previously traced. This gap seems to be causing a fair amount of non-ideal motion. During this time frame, the green dot has been deformed a significant amount compared with previous sequences. Slight shifts in the fluid's position towards the section where velocity effects are greatest explain this sudden stretching in the fluid.

Comparing the above two cases shows differing results due to a number of reasons. In the first run, the belts continually slipped during the first sequence of the run, resulting in an unsteady wall boundary velocity. Secondly, the initial locations and amount of each of the three dots differed slightly from the first to the second trials in comparing Figures 14 and 18. Differing amounts of tracer dye in somewhat different configurations will cause the dye to follow different streamlines in the flow which display slightly different behavior.
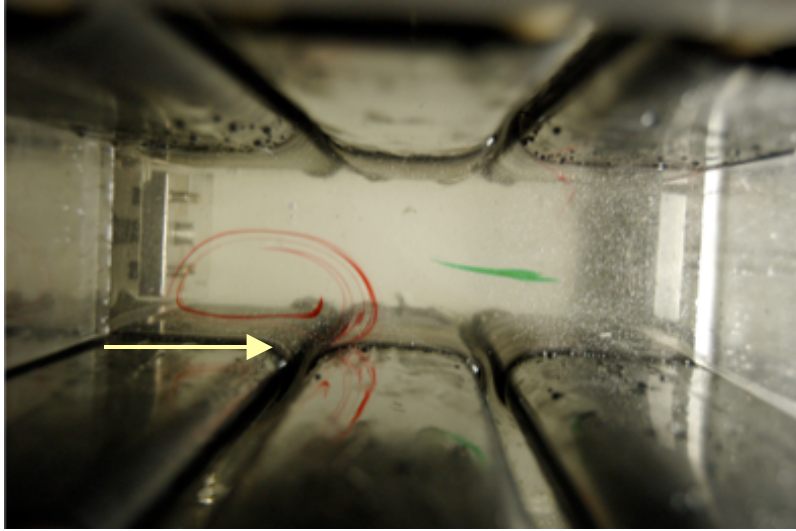
Figure 21. Results after operating tank for a total of six time periods in forward direction as indicated by the arrow.

Case III

For the third and final case tested, a different protocol is adopted. The purpose of this case was not only to test the second phase of the computer program, which changes the direction of the moving walls, but also to see if the flow is reversible. Starting from the initial conditions shown in Figure 22, the same boundary was moved to the right for the duration of one single period (Figure 23). The velocity was then reversed for one period to see if the dye spot ended up in the same location (Figure 24). After the boundary is run once in the reverse direction the experiment is run two times in a forward velocity configuration. This allows for comparison of the fluid motion for different starting locations, since the fluid did not return back to the original condition.
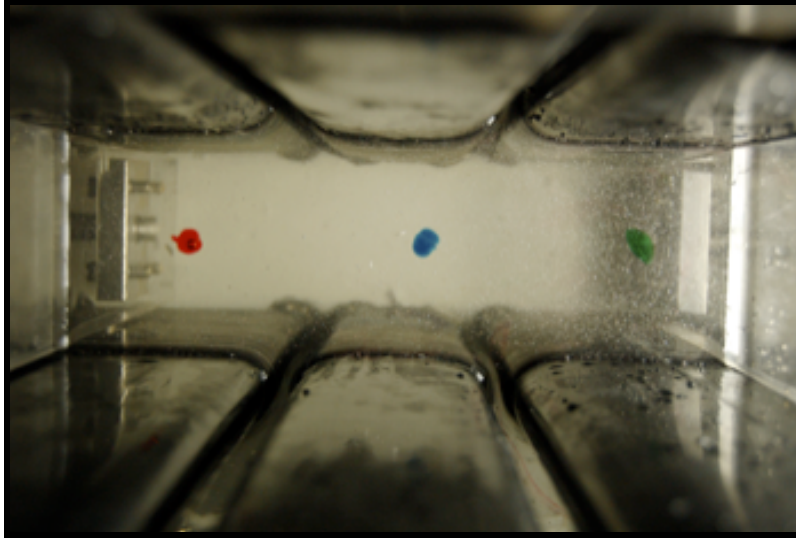
Figure 22. Initial locations of dye spots for the third and final case.
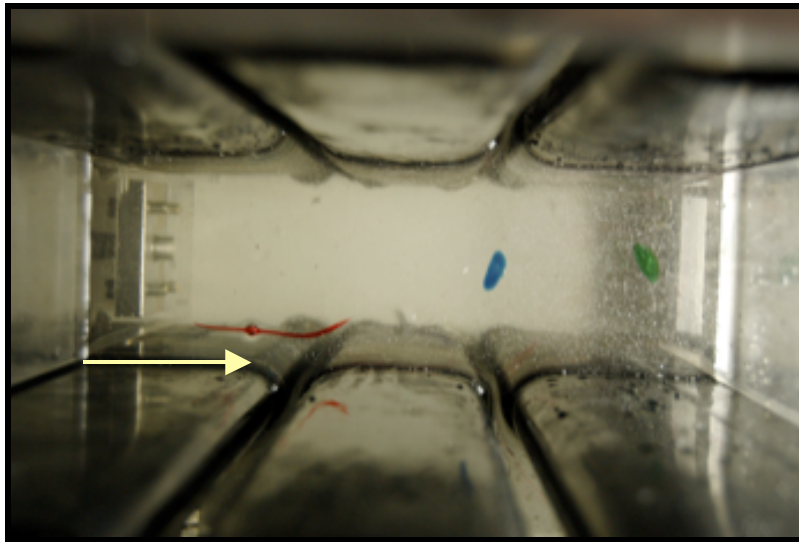
Figure 23. Positions of dyed glycerin after one time period of forward boundary motion.
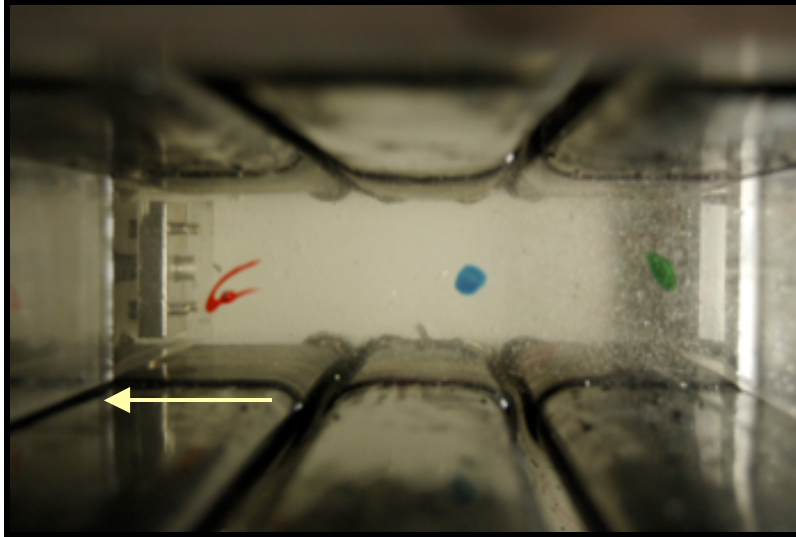
Figure 24. Image after flow in Figure 23 is reversed and to determine reversibility effects should be compared with Figure 22.

If the flow were completely reversible the spots in Figure 24 should exactly match their originating spots from Figure 22. However, this only occurs in Stokes flow, which unfortunately is not the case in the left side of the tank due to the higher operating Reynolds number. Moving to the right, the velocities are much less since there are no moving boundaries in these regions. This is seen from the small movements in the blue and green dots. These smaller velocities result in a smaller Reynolds number closer to the Stokes flow assumption and thus should be reversible.

Proceeding from the final locations in Figure 24, the tank is run twice with a forward velocity with images taken after each period (Figures 25 and 26). After this period there is a slight motion of the blue spot towards the right, while very little motion in the green dyed fluid. The red fluid starts its half circle trace in a counter clockwise direction.

After the second period, there is little change in the blue and green spots. The blue moves further to the right, opposite of what we had seen before, while the green spot looks larger than in the previous photos. Since the dyed fluid is made from a mix of water-based food coloring and glycerin, this is likely due to diffusion. Although originating in a different location, the red dye still traces a similar trajectory to those shown in the previous two cases. Figure 25 is the best depiction of the particle motion before a significant amount of fluid escapes the center region.
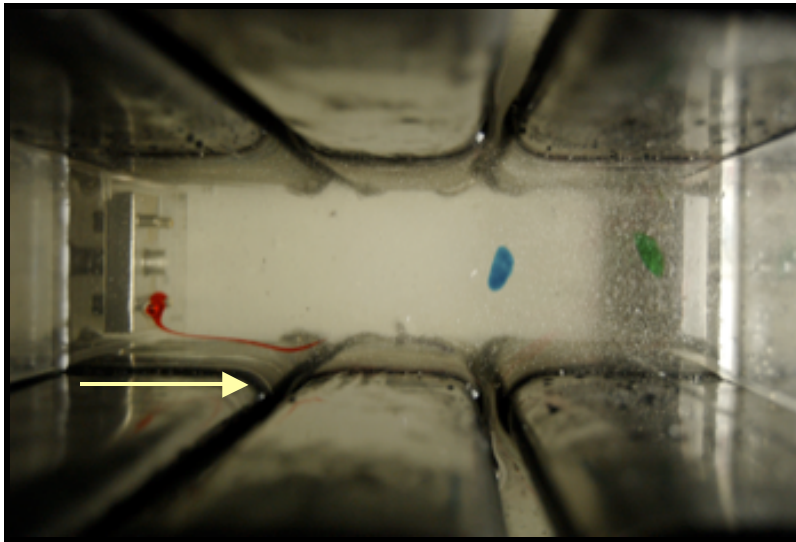
Figure 25. Dye positions after the flow is reversed for one full period. The original starting locations are shown in Figure 23.
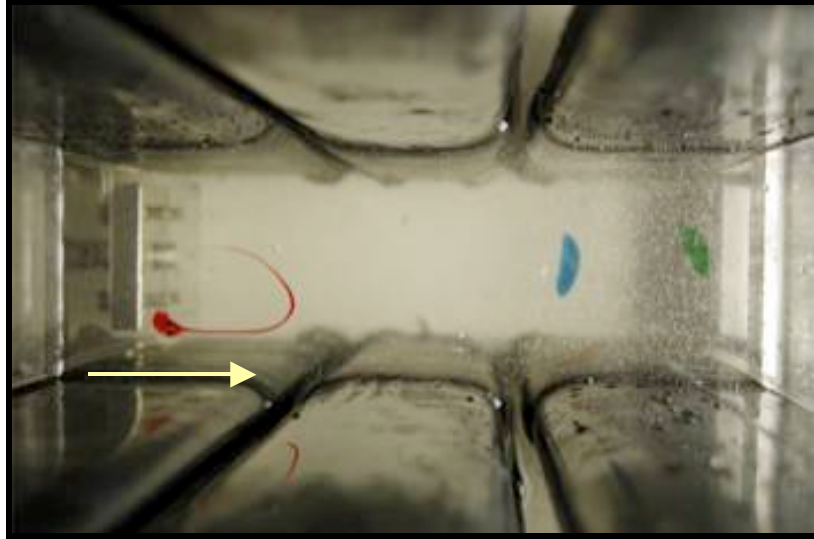
Figure 26. Position of dye tracers after two periods of forward boundary motion where the initial positions are shown in Figure 24.

CHAPTER IV

CONCLUSION

The objective of this study was to develop and test a device that produces lid-driven cavity flow capable of generating topological chaos. Chapter 2 discussed the physical tank and computer control program that were designed with the overall objective in mind. The simple case of one moving boundary was the focus of these experimental tests. Chapter 3 provided and discussed three successful cases for a preliminary study using one moving boundary.

The experiments conducted in this research have given insight into a different approach using a lid-driven cavity flow system. Using a qualitative approach, the displacements of fluid particles were tracked providing information on fluid flow for the motion of a single discontinuous boundary. Although this research did not generate topological chaos in a lid-driven cavity, there are many significant conclusions that can be drawn from this work. First consider the geometry, consisting of a test region with six discontinuous boundaries. Although only the motion of one boundary was defined in the cases presented in this paper, it was designed with the ability to move six discontinuous walls simultaneously. Secondly, these motions are the first example of lid-driven cavity flow that uses the concept of creating stirrers with periodic points in the flow. Under certain velocity distributions this geometry creates two separate stirring protocols, yielding entirely different outcomes. The LabVIEW program developed for this research

can be modified to accommodate for experiments using the new geometry. With only two moving boundaries and minor program modifications the new design will be able to create topological chaos.

Much thought was given to troubleshooting potential problems before the cases were conducted. Even with the improvements made to the system the design was unable to yield completely accurate results. The biggest problem stemmed from the gaps between the adjacent boundaries. Because of the design of the system and the physical components used to build the system, these gaps could not be minimized. Steps were taken to try to reduce the amount of fluid that moves between these walls, but as seen above in the results, these steps were insufficient to prevent the motion of glycerin out of the center test region. The fluid flux complicated the flows dynamics and weighed heavily in the outcome of the experiments, in the sense that the streamlines hypothesized were not found.

In order to eliminate these problems a different, more simplistic geometry has been proposed that should produce the same stirring protocols to be created [6]. Rather than six moving boundaries, this new geometry consists of a different aspect ratio with only two moving boundaries. A few recommendations can be made for the design and fabrication of this new system, based on some of the concerns identified in this research. First, because the test fluid acts as a lubricant between the moving walls and the driving rods, it is suggested that the system have one of the following: either use teeth that allow the rods and neoprene to fit snugly together, or gnurl the rods and use a gritty material on the inside surface of the neoprene. This way, when the rods drive the boundaries they are guaranteed not to slip and provide instantaneous motion once the motors begin moving.

Secondly, bearings should be used on both the top and bottom ends of each rod, with sealed bearings being used for ends that are submerged in glycerin. This will prevent the bearings from corroding while providing a smooth transition in the belt velocities and decreasing the amount of torque required to initialize motion in the motors.

Another suggestion in the design of the new system is to establish a different way to tighten the belts to the moving rods. In the current configuration, the tension rods were located on the inside of the tank with the adjustments located on the exterior of the tank. This was a problem because the neoprene boundaries had a tendency to creep up and down the rods if the tension rods were not adjusted symmetrically. These adjustment mechanisms occasionally caught the moving walls, stalling or even ripping the moving walls. One suggestion would be to make these mounts flush with the bottom of the tank. If the adjusters are flush and the boundary moves down towards them they will only skim the bottom of the tank and minimize the chance of ripping the neoprene. The top tensioning system does not have to be the same as the bottom, just as long as it provides the same amount of adjustment capability as the bottom.

The last suggestion is to build the top cover out of a piece of clear acrylic and construct it as simply as possible using the smallest number of parts. This will allow the entire inside of the tank to be viewed from above. Once the current tank design is closed and ready to run, the only visible section is the 8.75 inch cut-out in the top (Figure 4) and the side viewing walls (Figures 6 and 7). However, if the entire top were to be constructed out of a clear, durable material, it would increase visibility and provide more light for photographing the center test cavity.

APPENDIX A
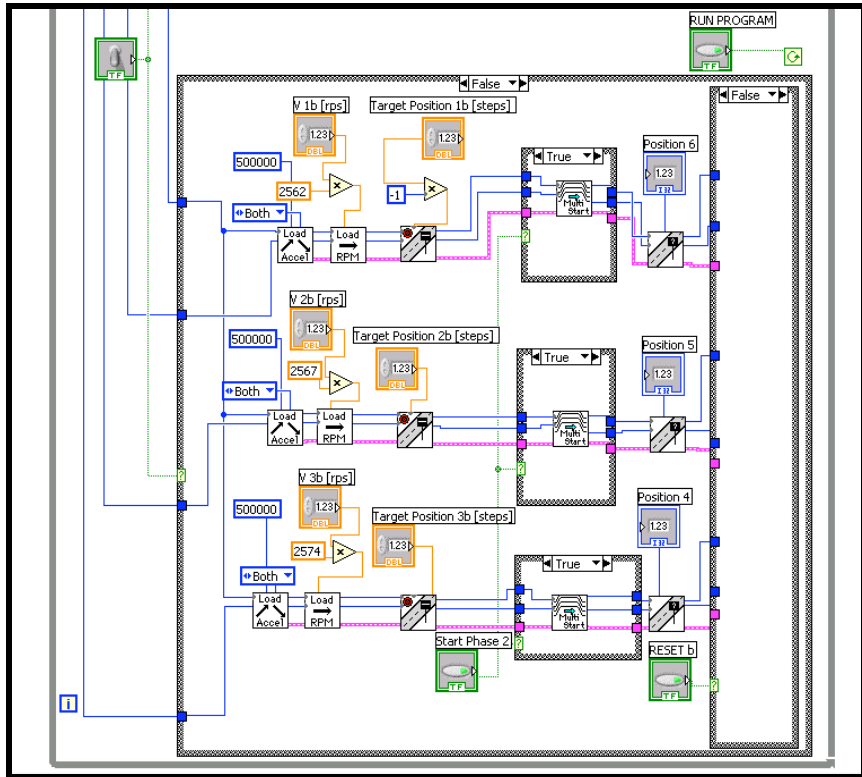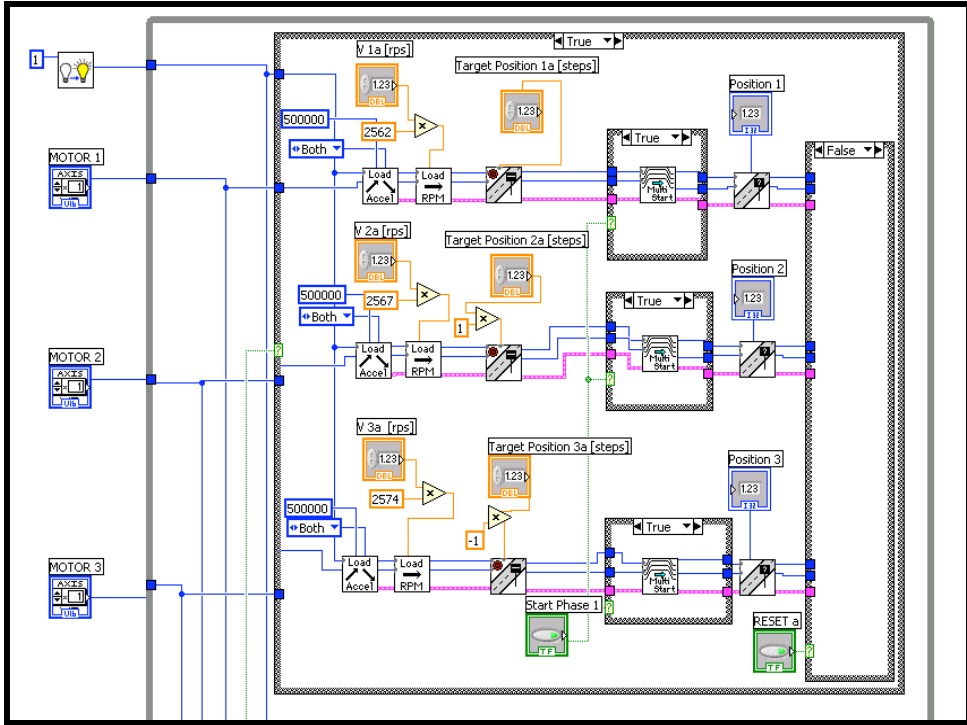
Stepper and Servo Motor Drives

NI MID-7604, NI MID-7602

- High-efficiency, bipolar chopper stepper drives
- User-selectable microstepping and peak current
- Integrated power supply
- CE approved and UL recognized

NI MID-7654, NI MID-7652

- High-efficiency servo amplifiers
- User-selectable peak current and continuous current
- Integrated power supply
- CE approved and UL recognized

Overview and Applications

The National Instruments MID-760x integrated stepper motor power drives and MID-765x integrated DC-brush servo motor power drives offer reliable, easy-to-connect drive solutions for National Instruments motion controllers. The NI MID-760x provides stepper motor control from the NI 7330, 7340, and 7350 controllers. The MID-7650 provides DC-brush servo motor control from NI 7340 and 7350 controllers. Because the MID-760x and the MID 7650 have all the required motion drive and motion I/O signals, they offer all the features of a universal motion interface wiring module with the enhancements of a powered motor drive in a single product. The NI MID power drives connect to motion controller boards through a single-shielded cable that transfers all motor commands, as well as motion I/O control and feedback signals.

The MID-7604 and MID-7602 are 4-axis and 2-axis stepper motor drive units, respectively. The MID-7654 and MID-7652 are 4-axis and 2-axis DC-brush servo motor drive units, respectively.

These compact, well integrated drives incorporate per-axis amplifiers, motor-power DC bus supplies, low-voltage motion I/O supplies, and pluggable screw terminal connectivity in a single rugged metal enclosure. This optimized system wiring design simplifies motion component selection.

High-Efficiency Architecture

The MID-760x power drives incorporate an efficient bipolar chopper architecture that converts step and direction control signals into winding currents for 2-phase stepper motors. The MID-765x power drives incorporate an efficient servo amplifier architecture that converts analog control signals into winding currents for DC-brush motors. The pulse width modulation driver technology in the MID-765x accurately controls motor winding current, while reducing motor heating, lowering ripple current, and improving overall motor performance. Active fan cooling provides optimal motion power drive operation.

Model	Stepper	Servo	NI 7300	NI 7350 NI 7340	(W)	Motor Drive (A)	Compact Current/Axis Diagnostic LEDs	Front Panel Enclosure and Microstepping	Front Panel Selectable Peak Current	Selectable Axes
MID-7604	✓	–	✓	✓	24	0.2 to 1.4	✓	✓	✓	4
MID-7602	✓	–	✓	✓	24	0.2 to 1.4	✓	✓	✓	2
MID-7654	–	✓	–	✓	48	0.8 to 5 continuous 10 peak	✓	–	✓	4
MID-7652	–	✓	–	✓	48	0.8 to 5 continuous 10 peak	✓	–	✓	2

Figure 1. Stepper and Servo Motor Drive Features

46

Stepper and Servo Motor Drives

Ordering Information

NI MID-7604 (4-axis stepper) 777936-0P
NI MID-7602 (2-axis stepper) 778003-0P
NI MID-7654 (4-axis servo) 778005-0P
NI MID-7652 (2-axis servo) 778004-0P
Cables
  Refer to the cable guide on page 645.

Accessories
Rack-Mount Kit
  MID-760x...777665-01
  MID-765x...187374-01
Strain-Relief Bar for MID-76xx............................187407-01
Panel-Mount Kit 187243-01

BUY ONLINE!
Visit *ni.com/info* and enter *mid7602*, *mid7604*, *mid7652*,
and/or *mid7654*.

Specifications

The specifications below apply to only the MID-76xx. Please refer to your controller specifications to determine overall system specifications.

Some signals define compatibility as pass-through. This means the MID-76xx may have passive filtering on these signals, but the signals do not affect the voltage range. Consult your motion controller specifications to determine allowable voltage range and logic level compatibility of the signal.

MID-7604, MID-7602 Stepper Motor Drives

Driver type	IM481H modular hybrid, bipolar chopper
Chopping operating frequency	20 kHz
Motor bus voltage	24 VDC nominal
Current per phase	0.2 to 1.4 A_{pk} (0.14 to 1 A_{rms}) (factory setting is 0.2 A_{pk})
Microstepping selections	x2, 4, 8, 16, 32, 64, 128, 256 x5, 10, 25, 50, 125, 250

Power Supply

Input voltage	90–132 VAC/204–264 VAC, 47–63 Hz
Input fuse	1.5 A, 230 VAC; 3 A, 115 VAC
Input fuse dimensions	5 x 20 mm

Host Bus Voltage Interlock

PC bus host voltage monitoring range	5 VDC

Physical

Dimensions	30.6 by 25.4 by 4.4 cm (12.1 by 10.0 by 1.7 in.)
Weight	4.5 kg (10 lb)

MID-7654, MID-7652 Servo Motor Drives

Driver type	Elmo Motion Control VIO 10/100
Peak current limit	1.7 to 10 A (default 1.7 A)
Continuous current limit	0.8 to 5 A (default 0.5 A)
DC-bus motor voltage	48 VDC nominal
Continuous power (all axes combined)	480 W at 25% duty cycle

Power Supply

Input voltage	90–132 VAC/198–264 VAC, 47–63 Hz
Input fuse	6 A, 230 VAC; 8 A, 115 VAC
Input fuse dimensions	0.25 by 1.25 in.

Host Bus Voltage Interlock

PC bus host voltage monitoring range	5 VDC ±5%

Physical

Dimensions	30.6 by 25.4 by 8.8 cm (12.0 by 10.0 by 3.5 in.)
Weight	10.2 kg (22.5 lb)

General (All MID 76xx drives)

Encoder Interface (Each Axis)

Inputs	Quadrature, incremental
Differential input threshold	±0.3 V (typical)
Single-ended input threshold	TTL/CMOS
Voltage range	0 to 5 VDC
Maximum quadrature frequency	20 MHz

Inhibit, Limit, and Home Switch Inputs (Each Axis)

Voltage range	0 to 12 VDC
Compatibility	Signal pass-through

Trigger Input

Noise filter (RC time constant)	100 ns
Compatibility	Signal pass-through

Breakpoint Output

Compatibility	Signal pass-through

Analog Input

Noise filter (RC time constant)	10 µs
Compatibility	Signal pass-through

Analog Output

Compatibility	Signal pass-through

Safety

Installation category II, pollution degree 2
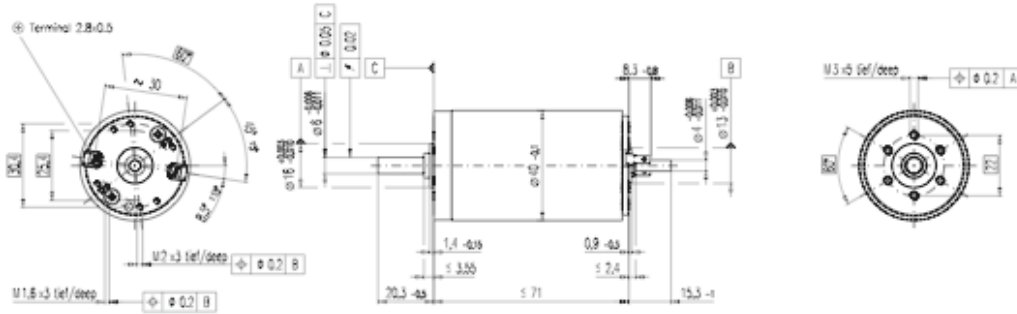
Environment

Operating temperature	0 to 50 °C for 765x, 0 to 45 °C for 760x
Storage temperature	-20 to 70 °C
Relative humidity	10% to 90% (noncondensing)

47

RE 40 ⌀40 mm, Graphite Brushes, 150 Watt

maxon DC motor

M 1:2

Stock program
Standard program
Special program (on request!)

Order Number

		148866	148867	148877	218008	218009	218010	218011	218012	218013	218014	218015
Industrial version		263065	263066	263067	263068	263069	263070	263071	263072	263073	263074	263075

Motor Data

1	Assigned power rating	W	150	150	150	150	150	150	150	150	150	150	150
2	Nominal voltage	Volt	12.0	24.0	48.0	48.0	48.0	48.0	48.0	48.0	48.0	48.0	48.0
3	No load speed	rpm	6920	7580	7580	6420	5560	3330	2690	2130	1710	1420	987
4	Stall torque	mNm	1690	2290	2500	1990	1580	996	796	641	512	415	289
5	Speed / torque gradient	rpm / mNm	4.11	3.32	3.04	3.23	3.53	3.36	3.39	3.35	3.37	3.44	3.45
6	No load current	mA	241	137	69	54	44	22	17	13	10	8	5
7	Starting current	A	103	75.9	41.4	28.0	19.2	7.26	4.69	3.00	1.92	1.29	0.627
8	Terminal resistance	Ohm	0.117	0.316	1.16	1.72	2.50	6.61	10.2	16.0	24.9	37.1	76.6
9	Max. permissible speed	rpm	8200	8200	8200	8200	8200	8200	8200	8200	8200	8200	8200
10	Max. continuous current	A	6.00	6.00	3.33	2.75	2.41	1.41	1.13	0.904	0.725	0.594	0.414
11	Max. continuous torque	mNm	98.7	181	201	196	198	193	192	193	193	191	190
12	Max. power output at nominal voltage	W	285	440	491	332	255	86.5	55.7	35.6	22.9	15.3	7.40
13	Max. efficiency	%	88	91	92	91	91	89	88	87	86	85	83
14	Torque constant	mNm / A	16.4	30.2	60.3	71.3	82.2	137	170	214	266	321	461
15	Speed constant	rpm / V	581	317	158	134	116	69.7	56.2	44.7	35.9	29.8	20.7
16	Mechanical time constant	ms	6	5	4	4	4	4	4	4	4	4	4
17	Rotor inertia	gcm²	135	134	134	125	127	118	117	118	117	114	114
18	Terminal inductance	mH	0.02	0.08	0.33	0.46	0.61	1.70	2.62	4.14	6.40	9.31	19.20
19	Thermal resistance housing-ambient	K / W	4.7	4.7	4.7	4.7	4.7	4.7	4.7	4.7	4.7	4.7	4.7
20	Thermal resistance rotor-housing	K / W	1.9	1.9	1.9	1.9	1.9	1.9	1.9	1.9	1.9	1.9	1.9
21	Thermal time constant winding	s	41	40	40	38	38	36	35	35	35	34	34

Specifications

- Axial play 0.05 - 0.15 mm
- Max. **ball bearing** loads
  axial (dynamic)
  - not preloaded 5.6 N
  - preloaded 2.4 N
  - radial (5 mm from flange) 28 N
  - Force for press fits (static) 110 N
  - (static, shaft supported) 1200 N
- Radial play **ball bearing** 0.025 mm
- Ambient temperature range -20 ... +100°C
- Max. rotor temperature +155°C
- Number of commutator segments 13
- Weight of motor 480 g
- 2 pole permanent magnet
- Values listed in the table are nominal.
  For applicable tolerances see page 43.
  For additional details please use the maxon
  selection program on the enclosed CD-Rom.

Operating Range

150 Watt
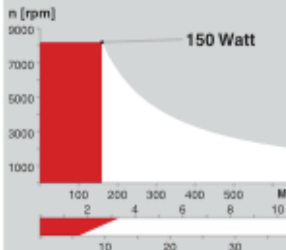
Comments   Details on page 49

Recommended operating range

Continuous operation
In observation of above listed thermal resistances (lines 19 and 20) the maximum permissible rotor temperature will be reached during continuous operation at 25°C ambient.
= Thermal limit.

Short term operation
The motor may be briefly overloaded (recurring).

148877 Motor with high resistance winding
148866 Motor with low resistance winding

maxon Modular System   Overview on page 17 - 21

Planetary Gearhead
⌀42 mm
3 - 15 Nm
Details page 218

Planetary Gearhead
⌀52 mm
4 - 30 Nm
Details page 221

Recommended Electronics:
ADS 50/5   page 253
ADS 50/10   253
ADS_E 50/5, 50/10   254
EPOS 24/5, 70/10   263
MIP 50, MIP 100   265
Notes   17

Digital MR Encoder
256 - 1024 CPT,
3 channels
Details page 233

Digital Encoder
HP HED_55_
500 CPT, 3 channels
Details page 236 / 238

Brake
⌀40 mm,
24 VDC, 0.4 Nm
Details page 269

Industrial version Encoder
Details page 241

Brake
Details page 270

82 maxon DC motor

July 2004 edition / subject to change

maxon motor

maxon motor control	**Choke Module**
	Order number 137303
Technical Documentation	**June 1999 Edition**

Choke Module

The choke module contains **3 linear storage chokes**. Thus it is particularly suitable for the combination with three-phased EC motors. With DC motors, the chokes are used in series or parallel connection. The storage choke increases the motor terminal inductance ⇒ smaller current ripple in PWM-(Pulse width modulation) operation.

Technical Data per Linear Storage Choke

Electrical data
- Nominal DC current $I_N =$ 5   A
- Inductance at I_N $L =$ 250   μH
- DC current resistor $R_{Cu} =$ 50   mΩ
- Max. current ripple $\Delta I =$ 0.2 I_N
- Max. frequency $f <$ 100   kHz

Temperature range   Operation   -25 ... 70°C

Humidity range   20 ... 75 % non condensating

Mechanical data
- Weight: 250 g
- Dimensions: Length   90 mm
       Width   70 mm
       Height   49 mm
- Mounting plate: for 4 screws M3
       Distance between threads   80 x 54 mm

Connections
- PCB-clamps   3 poles
  pitch   5 mm
  suitable for cable profile
  multiple-stranded wire   0.14 - 2.5 mm²
  single wire   0.14 - 4.0 mm²

Dimension Drawing

Dimensions in [mm]
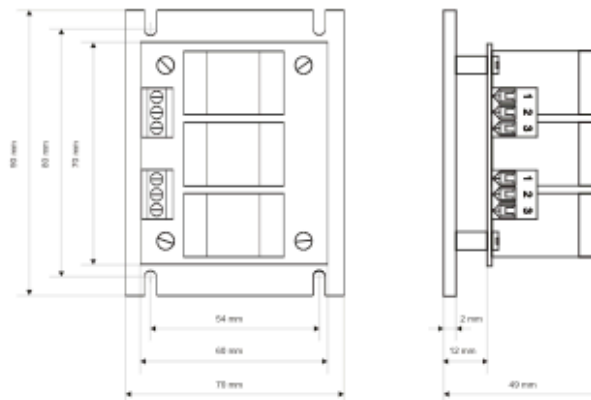
The latest edition of this operating instructions may be downloaded from the internet as a PDF-file under http://www.maxonmotor.com, category «Service», subdirectory «Downloads», order number 137303.

Digital Encoder HEDL 55__ with Line Driver RS 422

Stock program
Standard program
Special program (on request!)

Order Number		
110512	110514	110516

Type				
Shaft diameter	mm	3	4	6

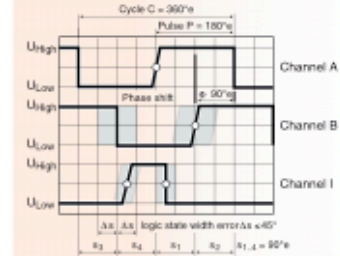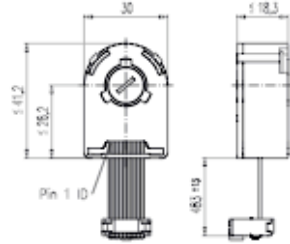| Combination							
+ Motor	Page	+ Gearhead	Page	+ Brake	Page	Overall length [mm] / ● see: + Gearhead	
F 2260, 40 W	94					111.9	
F 2260, 40 W	94	GP 62, 8.0 - 50 Nm	203			●	
F 2260, 80 W	95					147.4	
F 2260, 80 W	95	GP 62, 8.0 - 50 Nm	203			●	
A-max 26	114-120					63.5	
A-max 26	114-120	GP 26, 0.5 - 2.0 Nm	193			●	
A-max 26	114-120	GS 30, 0.07 - 0.2 Nm	194			●	
A-max 26	114-120	GP 32, 0.75 - 6.0 Nm	195/197			●	
A-max 26	114-120	GP 32, 0.4 - 2.0 Nm	199			●	
A-max 26	114-120	GS 38, 0.1 - 0.6 Nm	200			●	
A-max 32	122/124					82.3	
A-max 32	122/124	GP 32, 0.75 - 6.0 Nm	196/198			●	
A-max 32	122/124	GS 38, 0.1 - 0.6 Nm	200			●	
EC 32, 80 W	157					78.4	
EC 32, 80 W	157	GP 32, 0.75 - 6.0 Nm	196/198			●	
EC 40, 120 W	158					88.4	
EC 40, 120 W	158	GP 42, 3.0 - 15 Nm	201			●	
EC 40, 120 W	158	GP 52, 4.0 - 30 Nm	202			●	

Technical Data

Supply voltage	5 V ± 10 %
Output signal	EIA Standard RS 422
drivers used:	DS26LS31
No. of channels 2+1 Index Channel	(not at 1000 CPT)
Counts per turn	500 / 1000
Phase shift Φ (nominal)	90°e
Logic state width s	min. 45°e
Signal rise time (typical at C$_L$ = 25 pF, R$_L$ = 2.7 kΩ, 25°C)	180 ns
Signal fall time (typical at C$_L$ = 25 pF, R$_L$ = 2.7 kΩ, 25°C)	40 ns
Index pulse width (nominal) Option	90°e
Operating temperature range	0 ... +70°C
Moment of inertia of code wheel	≤ 0.6 gcm²
Max. acceleration	250 000 rad s⁻²
Output current per channel	min. -1 mA, max. 20 mA
Max. operating frequency	100 kHz

Pin Allocation for motor RE 75

Flanged connector
Type SOURIAU 8GM-QL2-12P
1 V$_{CC}$
2 N.C. (do not connect)
3 Gnd
4 N.C. (do not connect))
5 Channel I (Index)
6 Channel Ī
7 Channel B
8 Channel B̄
9 Channel A
10 Channel Ā
11 N.C. (do not connect))
12 N.C. (do not connect))
Recommended cable plug
Type SOURIAU 8GM-DM2-12S
(Metal, straight exit)
maxon Art. No. 2675.538) or
8G-V2-12S (plastic, 90° angle:
maxon Art. No. 2675.539)

Connection Example

Terminal resistance R = typical 100 Ω

April 2003 edition / subject to change

maxon tacho
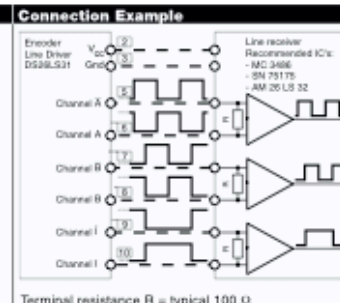
Planetary Gearhead GP 42 C ∅42 mm, 3 - 15 Nm
Ceramic Version

M 1:2
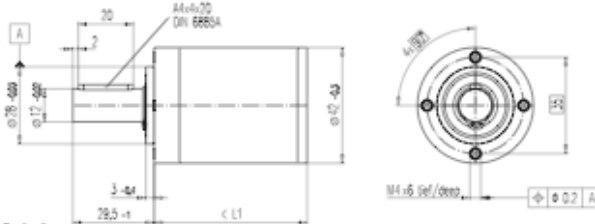
Technical Data

Planetary Gearhead	straight teeth
Output shaft	stainless steel
Bearing at output	ball bearing
Radial play, 12 mm from flange	preloaded
Axial play	preloaded
Max. permissible axial load	150 N
Max. permissible force for press fits	300 N
Recommended input speed	< 8000 rpm
Recommended temperature range	-20 ... +100°C

Number of stages	1	2	3	4
Max. perm. radial load, 12 mm from flange	120 N	150 N	150 N	150 N

Stock program
Standard program
Special program (on request!)

Order Number

Gearhead Data			203113	203115	203120	203125	203128	203134	203139
1	Reduction		3.5 : 1	12 : 1	43 : 1	91 : 1	150 : 1	319 : 1	546 : 1
2	Reduction absolute		$7/_2$	$49/_4$	$343/_8$	91	$2401/_{16}$	$637/_2$	546
3	Mass inertia	gcm²	14	15	15	15	15	15	14
	Order Number		203114	203116	203121	203126	203130	203135	203140
1	Reduction		4.3 : 1	15 : 1	53 : 1	113 : 1	186 : 1	353 : 1	676 : 1
2	Reduction absolute		$13/_3$	$91/_6$	$637/_{12}$	$339/_3$	$4459/_{24}$	$28561/_{81}$	676
3	Mass inertia	gcm²	9.1	15	15	9.4	15	9.4	9.1
	Order Number			203117	203122	203127	203131	203136	203141
1	Reduction			19 : 1	66 : 1	126 : 1	230 : 1	394 : 1	756 : 1
2	Reduction absolute			$169/_9$	$1183/_{18}$	126	$3281/_{16}$	$1183/_3$	756
3	Mass inertia	gcm²		9.4	15	14	15	15	14
	Order Number			203118	203123	203129	203132	203137	203142
1	Reduction			21 : 1	74 : 1	156 : 1	257 : 1	441 : 1	936 : 1
2	Reduction absolute			21	$147/_2$	156	$1029/_4$	441	936
3	Mass inertia	gcm²		14	15	9.1	15	14	9.1
	Order Number			203119	203124		203133	203138	
1	Reduction			26 : 1	81 : 1		285 : 1	488 : 1	
2	Reduction absolute			26	$2197/_{27}$		$15379/_{54}$	$4394/_9$	
3	Mass inertia	gcm²		9.1	9.4		15	9.4	
4	Number of stages		1	2	3	3	4	4	4
5	Max. continuous torque at gear output	Nm	3.0	7.5	15	15	15	15	15
6	Intermittently permissible torque at gear output	Nm	4.5	11.3	22.5	22.5	22.5	22.5	22.5
7	Max. efficiency	%	90	81	72	72	64	64	64
8	Weight	g	260	360	460	460	560	560	560
9	Average backlash no load	°	0.3	0.4	0.5	0.5	0.5	0.5	0.5
10	Gearhead length L1	mm	40.9	55.4	69.9	69.9	84.4	84.4	84.4

overall length   overall length

Combination:

+ Motor	Page	+ Tacho / Encoder	Page	+ Brake	Page	Overall length [mm] = Motor length + gearhead length + (tacho / encoder / brakes) + assembly parts						
RE 35, 90 W	80					111.9	126.4	140.9	140.9	155.4	155.4	155.4
RE 35, 90 W	80	MR Encoder	213			123.3	137.8	152.3	152.3	166.8	166.8	166.8
RE 35, 90 W	80	Digital Encoder HED_55_	216/218			132.9	147.4	161.9	161.9	176.4	176.4	176.4
RE 35, 90 W	80	DC-Tacho 22	224			130.0	144.5	159.0	159.0	173.5	173.5	173.5
RE 35, 90 W	80			Brake 40	248	148.0	162.5	177.0	177.0	191.5	191.5	191.5
RE 36, 70 W	81					112.2	126.7	141.2	141.2	155.7	155.7	155.7
RE 36, 70 W	81	MR Encoder	213			123.6	138.1	152.6	152.6	167.1	167.1	167.1
RE 36, 70 W	81	Digital Encoder HED_55_	216/218			133.2	147.7	162.2	162.2	176.7	176.7	176.7
RE 36, 70 W	81	DC-Tacho 22	224			130.3	144.8	159.3	159.3	173.8	173.8	173.8
RE 40, 150 W	82					112.0	126.5	141.0	141.0	155.5	155.5	155.5
RE 40, 150 W	82	MR Encoder	213			123.4	137.9	152.4	152.4	166.9	166.9	166.9
RE 40, 150 W	82	Digital Encoder HED_55_	216/218			132.7	147.2	161.7	161.7	176.2	176.2	176.2
RE 40, 150 W	82			Brake 40	248	148.1	162.6	177.1	177.1	191.6	191.6	191.6
RE 40, 150 W	82	Digital Encoder HED_55_	216/218	Brake 40	248	165.2	179.7	194.2	194.2	208.7	208.7	208.7
RE 40, 150 W	82	Digital Encoder HEDL 9140	220			166.1	180.6	195.1	195.1	209.6	209.6	209.6
RE 40, 150 W	82			Brake 28	249	156.1	170.6	185.1	185.1	199.6	199.6	199.6
RE 40, 150 W	82	Digital Encoder HEDL 9140	220	Brake 28	249	176.6	191.1	205.6	205.6	220.1	220.1	220.1
EC 40, 120 W	158					111.0	125.5	140.0	140.0	154.5	154.5	154.5
EC 40, 120 W	158	Digital Encoder HED_55_	217/219			129.4	143.9	158.4	158.4	172.9	172.9	172.9
EC 40, 120 W	158	Resolver 26	226			137.6	152.1	166.6	166.6	181.1	181.1	181.1
EC 40, 120 W	158			Brake 40	248	141.8	156.3	170.8	170.8	185.3	185.3	185.3
EC 45, 150 W	159					152.2	166.7	181.2	181.2	195.7	195.7	195.7
EC 45, 150 W	159	Digital Encoder HEDL 9140	220			167.8	182.3	196.8	196.8	211.3	211.3	211.3
EC 45, 150 W	159	Digital Encoder HEDL 9140	220	Brake 28	249	176.6	191.1	205.6	205.6	220.1	220.1	220.1
EC 45, 150 W	159	Resolver 26	226			152.2	166.7	181.2	181.2	195.7	195.7	195.7
EC 45, 150 W	159			Brake 28	249	159.6	174.1	188.6	188.6	203.1	203.1	203.1
EC 45, 250 W	160					185.0	199.5	214.0	214.0	228.5	228.5	228.5
EC 45, 250 W	160	Digital Encoder HEDL 9140	220			200.6	215.1	229.6	229.6	244.1	244.1	244.1
EC 45, 250 W	160	Digital Encoder HEDL 9140	220	Brake 28	249	209.4	223.9	238.4	238.4	252.9	252.9	252.9
EC 45, 250 W	160	Resolver 26	226			185.0	199.5	214.0	214.0	228.5	228.5	228.5
EC 45, 250 W	160			Brake 28	249	192.4	206.9	221.4	221.4	235.9	235.9	235.9

maxon gear 201

maxon gear

REFERENCES

1.   Aref, H. (1984) Stirring by chaotic advection. *Journal of Fluid Mechanics*, **143**, 1-21.

2.   Batchelor, G.K. An Introduction to Fluid Dynamics. Cambridge University Press, 1967.

3.   Bau, H.H., Zhong, J., and Yi, M. (2001) A minute magneto hydro dynamic (MHD) mixer. *Sensors and Actuators B*, **79**, 207-215.

4.   Boyland, P.L., Aref, H., and Stremler, M.A. (2000) Topological fluid mechanics of stirring. *Journal of Fluid Mechan*ics, **403**, 277-304.

5.   Bruneau, C.H. and Saad, M. (2006) The 2D lid-driven cavity problem revisited. *Computers & Fluids*, **35**, 326-348.

6.   Chen, J. and Stremler, M.A. (2006) Topological chaos in cavities and channels. *Bulletin of the American Physical Society*, **51** (9), p. 152.

7.   Chien, W.L., Rising, H., and Ottino, J.M. (1986) Laminar mixing and chaotic mixing in several cavity flows. *Journal of Fluid Mechanics*, **170**, 355-377.

8.   Finn, M.D., Thiffeault, J., and Gouillart, E. (2006) Topological chaos in spatially periodic mixers. *Physica D*, **221**, 92-100.

9.   Gaskell, P.H., Gürcan, F., Savage, M.D., and Thompson, H.M. (1998) Stokes flow in a double-lid-driven cavity with free surface side walls. Proceedings of the Institution of Mechanical Engineers. Part C, *Journal of Mechanical Engineering Science*, **212**, 387-403.

10.   Gouillart, E., Thiffeault, J., and Finn, M.D. (2006) Topological mixing with ghost rods. *Physical Review E*, **73**, 1-8.

11.   Gürcan, F. (2003) Streamline topologies in Stokes flow within lid-driven cavities. *Theoretical Computational Fluid Dynamics*, **17**, 19-30.

12.   Kuhlmann, H.C., Wanschura, M. and Rath, H.J. (1997) Flow in two-sided lid-driven cavities: non-uniqueness, instabilities and cellular structures. *Journal of Fluid Mechanics*, **336**, 267-299.

13.   Leriche, E., and Gavrilakis, S. (2000) Direct numerical simulation of the flow in a lid-driven cubical cavity. *Physics of Fluids*, **12**, 1363-1376.

14.   Ottino, J.M., Leong, C.W., Rising, H., and Swanson, P.D. (1988) Morphological structures produced by mixing in chaotic flows. *Nature*, **333**, 419-425.

15.   Ottino, J. M. The Kinematics of Mixing: Stretching, Chaos, and Transport. Cambridge University Press, 1989.

16.   Pan, F., and Acrivos, A. (1967) Steady flows in rectangular cavities. *Journal of Fluid Mechanics*, **28**, 643-655,

17.   Prasad, A.K., Koseff, J.R. (1989) Reynolds number and end-wall effects on a lid-driven cavity flow. *Physics of Fluids A,* **1**, 208-18.

18.   Schreiber, R., and Keller, H.B. (1983) Driven cavity flows by efficient numerical techniques. *Journal of Computational Physics*, **49**, 310-333.

19.   Shankar P.M. (1993) The eddy structure in Stokes flow in a cavity. *Journal of Fluid Mechanics*. **250**, 371-383

20.   Shankar, P.N., and Deshpande, M.D. (2000) Fluid Mechanics in the driven cavity. *Annual Review, Fluid Mechanics*, **32**, 93-136.

21.   Sturges, L.D. (1985) Stokes flow in a two-dimensional cavity with moving end walls. *Physics of Fluids*, **29**, 1731-1734.

22.   Vikhansky, A. (2004) Simulation of topological chaos in laminar flows. *Chaos*, **14**, 14-22.

23.   Weiss, R. F., and Florsheim, B.H. (1965) Flow in a cavity at low Reynolds number. *The Physics of Fluids*, **8**, 1631-1635.

24.   White, F.M. Viscous Fluid Flow 2nd edition. McGraw Hill,1991.